Topographic Rossby Waves in the Abyssal South China Sea

QI QUAN,[a] ZHONGYA CAI,[b,c] GUANGZHEN JIN,[d] AND ZHIQIANG LIU[a]

[a] *Department of Ocean Science and Engineering, Southern University of Science and Technology, Shenzhen, China*
[b] *State Key Laboratory of Internet of Things for Smart City, and Department of Civil and Environmental Engineering, University of Macau, Macau, China*
[c] *Center for Ocean Research in Hong Kong and Macau, Macau, China*
[d] *College of Marine Ecology and Environment, Shanghai Ocean University, Shanghai, China*

ABSTRACT: Topographic Rossby waves (TRWs) in the abyssal South China Sea (SCS) are investigated using observations and high-resolution numerical simulations. These energetic waves can account for over 40% of the kinetic energy (KE) variability in the deep western boundary current and seamount region in the central SCS. This proportion can even reach 70% over slopes in the northern and southern SCS. The TRW-induced currents exhibit columnar (i.e., in phase) structure in which the speed increases downward. Wave properties such as the period (5–60 days), wavelength (100–500 km), and vertical trapping scale (10^2–10^3 m) vary significantly depending on environmental parameters of the SCS. The TRW energy propagates along steep topography with phase propagation offshore. TRWs with high frequencies exhibit a stronger climbing effect than low-frequency ones and hence can move further upslope. For TRWs with a certain frequency, the wavelength and trapping scale are dominated by the topographic beta, whereas the group velocity is more sensitive to the internal Rossby deformation radius. Background circulation with horizontal shear can change the wavelength and direction of TRWs if the flow velocity is comparable to the group velocity, particularly in the central, southern, and eastern SCS. A case study suggests two possible energy sources for TRWs: mesoscale perturbation in the upper layer and large-scale background circulation in the deep layer. The former provides KE by pressure work, whereas the latter transfers the available potential energy (APE) through baroclinic instability.

KEYWORDS: Abyssal circulation; Mesoscale processes; Oscillations; Topographic effects

1. Introduction

In oceans worldwide, for example, along the mainstream of the Gulf Stream, in the Gulf of Mexico, and in the Arctic Ocean's Beaufort Gyre, the low-frequency variability of the deep current (below 1000 m) over steep topography is reportedly dominated by topographic Rossby waves (TRWs) with periods of several days to hundreds of days (e.g., Thompson and Luyten 1976; Thompson 1977; Hogg 1981, 2000; Johns and Watts 1986; Pickart and Watts 1990; Hamilton 1990, 2007, 2009; Peña-Molino et al. 2012; Zhao and Timmermans 2018; Hamilton et al. 2019). TRWs are thought to be excited by cross-isobathic motion when fluid columns are stretched and compressed over steep topography, for example, the deep fluctuations of the Gulf Stream and warm-core rings (Pickart 1995) or cross-isobath meander of deep eddies moving along slopes (Oey 2008). In the abyssal ocean, for example, at the Pacific Yap–Mariana Junction, which is the choke point of the northward transport route of the Pacific meridional overturning circulation (Siedler et al. 2004), energetic TRWs are believed to play an important role in modulating deep circulation (Ma et al. 2019), which can change the transport of heat and biogeochemical substances in the global ocean and hence affect the climate and ecosystem (Kawano et al. 2006; Chen and Tung 2014).

The South China Sea (SCS) is the largest marginal sea in the northwestern Pacific Ocean, where the deep basin is enclosed below 2000 m (Fig. 1). Like the Gulf of Mexico, the SCS provides suitable conditions for the generation of TRWs owing to a combination of complex topography (Huang et al. 2017), Loop Current (or eddy shedding) from western boundary current (WBC) intrusion (Nan et al. 2011, 2015), and eddies (Xiu et al. 2010; Chen et al. 2011). Shu et al. (2014) suggested that interactions between TRWs and planetary Rossby waves may be a mechanism for the deep upwelling associated with the meridional overturning circulation in the abyssal SCS. Moreover, TRWs and wave-related mixing effects cannot only govern the generation and evolution of deep circulation in the SCS (Quan and Xue 2019), but also affect the vertical coupling of the SCS circulation between the upper and middle layers by modulating the pressure field throughout the water column (Quan and Xue 2018; Cai and Gan 2020). Because the SCS circulation acts as an important link in heat and mass exchange between the Pacific and Indian Oceans (Qu et al. 2006; Yu et al. 2007; Gordon et al. 2012; Li et al. 2019), the modulation of the SCS circulation by TRWs may change the heat and water transport and affect the regional climate and ecosystem.

However, there was little research focusing on TRWs in the SCS in recent decades until Shu et al. (2016) reported pioneering observations near the Nansha Islands in the southern SCS. Their results revealed persistent and energetic TRWs below 1400 m with periods of 9–14 days and a wavelength of approximately 82 km. The wave-induced bottom current can

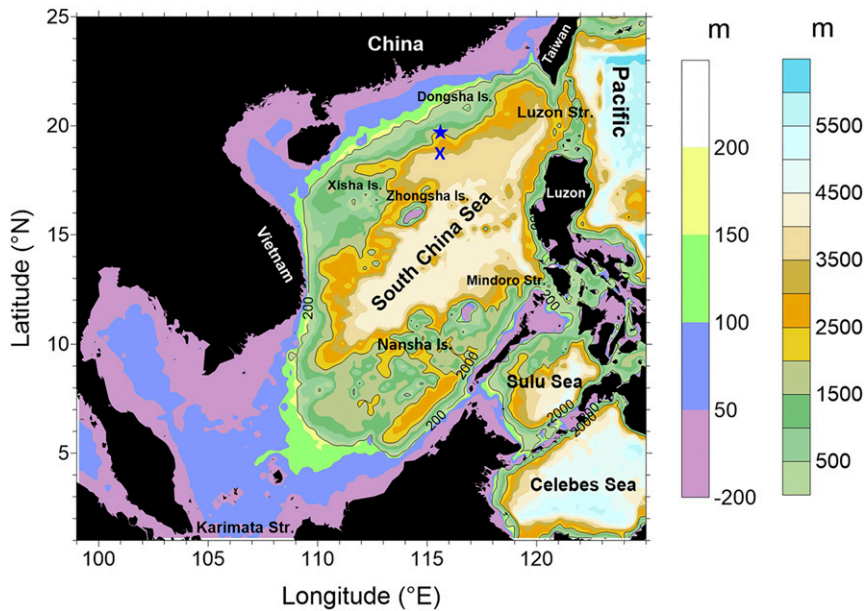*Corresponding author*: Zhiqiang Liu, liuzq@sustech.edu.cn

FIG. 1. Topography (m) of the SCS. Black solid lines denote the 200- and 2000-m isobaths. The blue star denotes the mooring site X.

be as large as approximately $10\,\mathrm{cm\,s^{-1}}$, which is one order of magnitude larger than the ambient deep flow. This finding implies that TRWs in areas of steep topography may play a role comparable to that of internal tides in modulating the deep SCS circulation. TRWs were also observed recently at two moorings over the slope of the northern SCS (Wang et al. 2019). The waves around the Dongsha Islands showed a peak spectral energy at approximately 14.5 days and can account for more than 40% of the total variance of the bottom velocity fluctuations. A ray tracing model indicated that the energy of TRWs propagated westward along the slope. Both Shu et al. (2016) and Wang et al. (2019) identified the energy source of TRWs in the SCS as mesoscale eddies in the upper layer. These eddies have a spatiotemporal scale similar to that of the waves and cause the deep-layer water column to cross the isobaths under the conservation of potential vorticity (PV).

These studies provide interesting insight into the interpretation of the variability of the deep flow and the relationships between currents in different layers of the SCS. However, because TRWs depend strongly on environmental parameters such as the topographic gradient, depth, and stratification (Reid and Wang 2004), too few observations are available to describe TRWs and their energy pathways in the entire SCS. Moreover, it was found that the background circulation in the Gulf of Mexico not only can provide energy to deep eddies by baroclinic instability and thus excite TRWs (Oey 2008), but also can effectively change the group velocity, wavelength, and direction of the waves (Oey and Lee 2002). Unlike the Gulf of Mexico or other large marginal seas, the SCS has a unique sandwich-like circulation system (i.e., cyclonic circulation in the upper and deep layers and anticyclonic circulation in the middle layer; separated by ~500 and ~2000 m), and significant

westward intensification occurs along the slope in each layer (Chen and Xue 2014; Xu and Oey 2014; Gan et al. 2016; Zhu et al. 2017; Cai et al. 2020). However, previous studies did not consider the effects of the SCS circulation on TRWs. Therefore, important issues remain to be addressed, such as the distributions of the wave properties (e.g., wavelength and period) and the wave energy paths in the entire deep SCS, as well as the connection between the TRWs and the SCS circulation. In this study, we attempted to answer these questions by analyzing the observations and high-resolution reanalysis data.

The rest of this paper is organized as follows. The data, TRW theory, and ray tracing model are briefly presented in section 2. Section 3 describes the basin-scale spatiotemporal features (e.g., the period, wavelength, and vertical trapping scale) of the deep-current variability in the SCS, which are used to identify typical TRWs. The propagations of TRWs in the abyssal SCS with and without considering the effect of the background circulation are investigated in section 4. A specific event is used as an example to illustrate possible sources of TRW energy in section 5. Finally, section 6 summarizes the study.

2. Data and methods

a. Data

Mooring site X (19.7°N, 115.6°E) was located on the slope southwest of the Dongsha Islands (blue star in Fig. 1), where the water depth is ~2000 m. The mooring was designed to observe the bottom flow and equipped with an upward-looking 600-kHz acoustic Doppler current profiler (ADCP). The sampling time interval was 30 min, and the vertical resolution was 5 m with four observational depths (1981.62, 1986.62, 1991.62, and 1996.62 m). Velocity profiles were continuously

recorded for about 8 months from 12 August 2011 to 12 April 2012, and the percentage of valid data was higher than 95%. Note that currents at four observational depths were basically in phase but decreased in magnitude downward (not shown). Hence, we use the data at the top level (1981.62 m; ~20 m above the bottom) for analysis to minimize the impact of bottom friction and better reveal the characteristics of TRWs.

The periods of TRWs are shorter than 100 days, and the temporal variation of the wave properties is determined mainly by the stratification, which changes slightly from year to year in the deep SCS. Therefore, the 6-yr data of the Hybrid Coordinate Ocean Model + Navy Coupled Ocean Data Assimilation (HYCOM + NCODA) global 1/12° Analysis (GLBv0.08; https://www.hycom.org/) from 2013 to 2018 cover a long enough period to resolve these subinertial waves and are used in this study. The system uses a 3D variational scheme to assimilate available satellite altimeter observations, satellite and in situ sea surface temperature, and in situ vertical temperature and salinity profiles from XBTs, Argo floats, and moored buoys (Cummings 2005; Cummings and Smedstad 2013). The 3-hourly data include the sea surface height, 3D horizontal velocity, temperature, and salinity. The horizontal resolution is about 8.4–9.2 km at 5°–25°N and there are 41 layers in the water column from 0 to 5500 m (1000, 1250, 1500, 2000, 2500, 3000, 4000, 5000, and 5500 m for the deep layer).

The HYCOM reanalysis data have been validated to well reproduce the multiscale physical processes in the world oceans and are widely used in the relevant energy analysis, such as the eddy available potential energy (APE) field in the global ocean, energetics of eddy–mean flow interactions in the Brazil Current, seasonal cycle of the eddy kinetic energy (EKE) in the Kuroshio Extension, and energy transfer underlying the eddy shedding from the Kuroshio intrusion in the northeastern SCS (Luecke et al. 2017; Magalhães et al. 2017; Yang and Liang 2018; Zhang et al. 2017). Different from the open oceans, the observations for assimilation are so limited in the SCS that HYCOM reanalysis in this region is close to a free-running case. Even so, the weakly assimilative HYCOM reanalysis can still reproduce the abyssal SCS circulation better than other seven quasi-global model products (Xie et al. 2013). Moreover, the presence of TRWs in the deep SCS had been revealed by Shu et al. (2014) using the 7-yr data of HYCOM GLBa0.08. The latest GLBv0.08 has a higher vertical and temporal resolution than GLBa0.08, and hence is believed to be reliable for our study.

b. TRW dynamics

The linear TRW theory was first derived by Rhines (1970). The governing equation is the linear quasigeostrophic PV equation

$$\frac{\partial}{\partial t}\left[P_{xx} + P_{yy} + \left(\frac{f}{N}\right)^2 P_{zz}\right] + \beta P_x = 0, \tag{1}$$

where x and y denote east and north, respectively; z is positive upward; P is the pressure; $f = f_0 + \beta y$ is the Coriolis parameter; $\beta = \partial f/\partial y$ is the planetary beta; and N is the Brunt–Väisälä frequency. The associated boundary conditions are a rigid lid and no normal flow through the bottom:
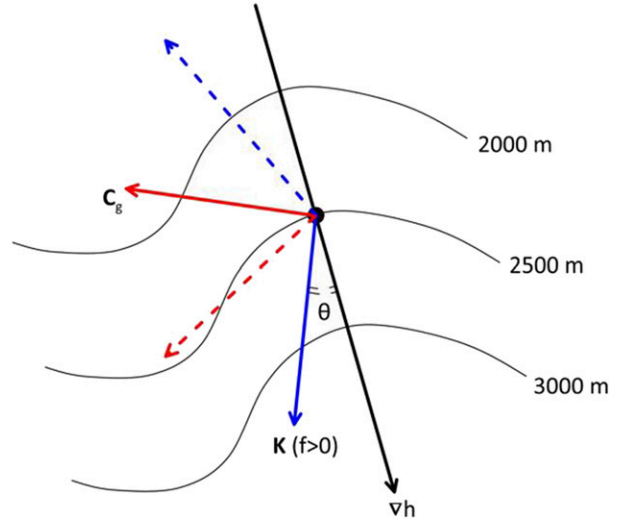

FIG. 2. Schematic of the relationships among the topographic gradient ∇h (black vector), wavenumber vector $\mathbf{K}$ (blue vector), and group velocity $\mathbf{C}_g$ (red vector) in the Northern Hemisphere when $NhK/f \approx O(1)$ or larger. The term θ is the clockwise angle between $\mathbf{K}$ and ∇h. The wavenumber vector $\mathbf{K}$ is nearly perpendicular to the group velocity $\mathbf{C}_g$. The group velocity $\mathbf{C}_g$ points upslope when $\mathbf{K}$ points downslope for $0 < \theta < \pi/2$ (solid vectors), and vice versa for $\pi/2 < \theta < \pi$ (dashed vectors).

$$\frac{\partial}{\partial t}p_z = 0 \qquad \text{at} \quad z = 0, \quad \text{and} \tag{2}$$

$$\frac{\partial}{\partial t}p_z = \frac{N^2}{f_0}(p_x h_y - p_y h_x) \quad \text{at} \quad z = -h. \tag{3}$$

A solution of the form

$$p = A(z)e^{i(kx+ly-\omega t)} \tag{4}$$

is substituted into Eq. (1), and Eqs. (2) and (3) are used to obtain two coupled equations:

$$\lambda_\nu^2 = \left(k^2 + l^2 + \frac{\beta k}{\omega}\right)\left(\frac{N}{f}\right)^2, \quad \text{and} \tag{5}$$

$$\omega = K|\nabla h|\sin(\theta)\frac{N^2}{\lambda_\nu f}\coth(\lambda_\nu h), \tag{6}$$

where λ_ν^{-1} is the vertical trapping scale of the wave, $\mathbf{K} = (k, l)$ is the horizontal wavenumber vector, $K^2 = k^2 + l^2$, h is the water depth, $\nabla h = (h_x, h_y)$ is the topographic gradient, and ω is the frequency. For $f > 0$, θ is the clockwise angle between the wavenumber vector and the direction of the topographic gradient (i.e., $\nabla h/|\nabla h|$). To first order [$\tanh(\lambda_\nu h) \approx 1$ and $\beta = 0$], TRWs frequencies are independent of wavenumber magnitude (i.e., $\omega = N|\nabla h|\sin\theta$). Thus, the group velocity ($\mathbf{C}_g = \nabla_{\mathbf{K}}\omega$) and wavenumber vector $\mathbf{K}$ must be perpendicular to each other. As shown in Fig. 2, $\mathbf{C}_g$ is directed clockwise (upslope) with respect to $\mathbf{K}$ when the latter points downslope ($0 < \theta < \pi/2$) and anticlockwise (downslope) when $\mathbf{K}$ points upslope ($\pi/2 < \theta < \pi$).

c. Ray tracing model

To investigate TRW propagation in the deep SCS, we use a ray-tracing technique. Ray tracing models are widely used to identify TRWs and their energy sources (Pickart 1995; Oey and Lee 2002; Hamilton 2007, 2009; Wang et al. 2019). We modify the ray tracing model of Meinen et al. (1993) by considering the background flow. The model is under the Wentzel–Kramer–Brillouin (WKB) limit, where the environmentally induced changes in the wave amplitude and phase are assumed to vary at scales larger than the local wavelength. Following Oey and Lee (2002), the equations governing the ray path and wavenumber are given by

$$\frac{d\mathbf{x}}{dt} = \frac{\partial \omega}{\partial \mathbf{K}} = \mathbf{C}_g + \mathbf{v}_h, \quad \text{and} \tag{7}$$

$$\frac{d\mathbf{K}}{dt} = -\sum_{i=1}^{n} \frac{\partial \omega}{\partial E_i} \nabla E_i - k\nabla u - l\nabla v, \tag{8}$$

where $d/dt = (\partial/\partial t) + (\mathbf{C}_g + \mathbf{v}_h) \cdot \nabla$ is the derivative following the wavegroup, $\mathbf{x}$ is the location of the wavegroup (i.e., the energy ray), $\mathbf{v}_h = (u, v)$ is the horizontal background flow, and E_i denotes any of the environmental parameters N, h, h_x, and h_y (thus, $n = 4$ here) that result in refraction of the wave. Given the initial position, frequency, and wavenumber vector, Eqs. (7) and (8) can be integrated forward in time. Note that ω is constant along the ray path if the parameters have no time-dependence; thus, it not only constrains the ray path but also serves as a useful check on the numerical results.

3. Features of TRWs in the deep SCS

Using the theory of Rhines (1970), we investigate the deep-current variability to identify the most typical TRWs in the deep SCS by setting three validation conditions: 1) the in situ deep-layer energy falling into the TRW period range is significant; 2) the spatiotemporal structures of the deep-current fluctuations match the characteristics of TRWs; and 3) the frequency and wavenumber conform to the dispersion relation of TRWs. To evaluate the possible occurrences and parameters of TRWs, we use the smoothed topography and stratification in calculation to avoid the influence of small-scale variations (Hamilton 2007, 2009). We smooth the topography by using a Shapiro filter to eliminate small-scale undulations but retain large-scale terrain features. In the deep SCS, the buoyancy frequency N is a weak function of depth. Thus, the 6-yr-mean N averaged over the water column 200 m above the seabed is used here.

a. Deep circulation in the SCS

On the basis of the basin-integrated vorticity, the cyclonic circulation below 2000 m is conventionally defined as the deep SCS circulation (Wang et al. 2011; Lan et al. 2013; Wang et al. 2016). Figure 3 shows the 6-yr-mean circulation averaged from 2000 m to the bottom in the deep SCS on the basis of HYCOM GLBv0.08. Basin-scale cyclonic circulation with an intensified WBC clearly predominates in the deep SCS and involves interior subbasin-scale cyclonic and anticyclonic gyres. The depth-averaged currents in most areas are slower than $0.02\,\mathrm{m\,s^{-1}}$, whereas those along the deep western boundary can be as fast as
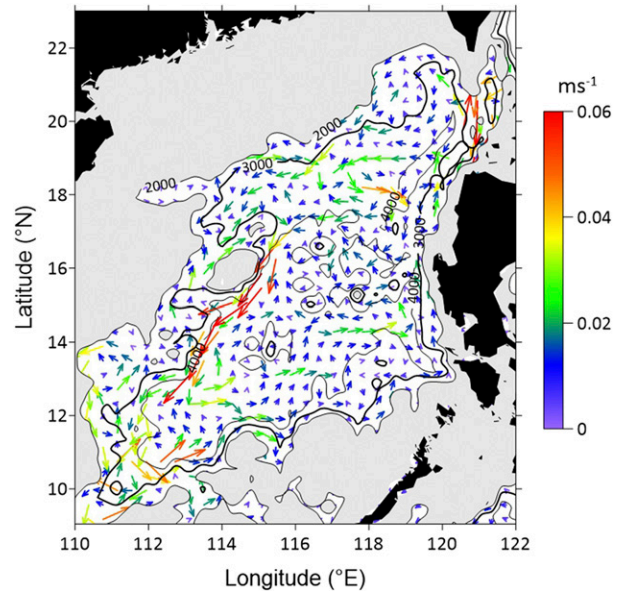

FIG. 3. 6-yr-mean deep circulation $(\mathrm{m\,s^{-1}})$ averaged from 2000 m to the bottom in the abyssal SCS based on HYCOM GLBv0.08 (2013–18).

$0.06\,\mathrm{m\,s^{-1}}$. The modeled deep WBC (DWBC) is probably overestimated relative to the value of $0.02\,\mathrm{m\,s^{-1}}$ observed by Zhou et al. (2017), but the axis position, core depth, and current width are similar (not shown). Although the mean circulation in the abyssal SCS appears very weak, it is not as quiet as it seems. Energetic low-frequency "noise" has been observed in the deep SCS circulation (Shu et al. 2016; Wang et al. 2019) and will be described in the following sections.

b. Period

The 8-month observations indicate persistent and energetic intraseasonal fluctuations of bottom flow at site X, consistent with the findings in the southeast of the Dongsha Islands (Wang et al. 2019). Despite strong contributions due to tides, the intraseasonal oscillations filtered at periods of 5–90 days account for 40.2% of the standard deviation (STD) of total kinetic energy (KE) at site X (Fig. 4a). Spectral analysis further indicates that the significant KE of intraseasonal oscillations over the 95% confidence level concentrates in the period band of 5–20 days (red solid line in Fig. 4b). Within this significant period band, the STD ellipse of bottom velocity shows a small oblateness with the major principal axis (about $0.02\,\mathrm{m\,s^{-1}}$) parallel to the local isobath (red ellipse in Fig. 4c).

In conjunction with the observations, we use HYCOM GLBv0.08 to reveal the deep-flow variability over the entire SCS. Except for a weaker intensity in power spectrum density (PSD), the HYCOM reanalysis can generally reproduce the subinertial motions within the frequency band similar to the observations (blue solid line in Fig. 4b). Regardless of tidal effects, the modeled intraseasonal fluctuations can account for 54.3% of the STD of total bottom KE at site X. The modeled STD ellipse of bandpassed bottom velocity is basically oriented in the same direction as the observations, with a comparable
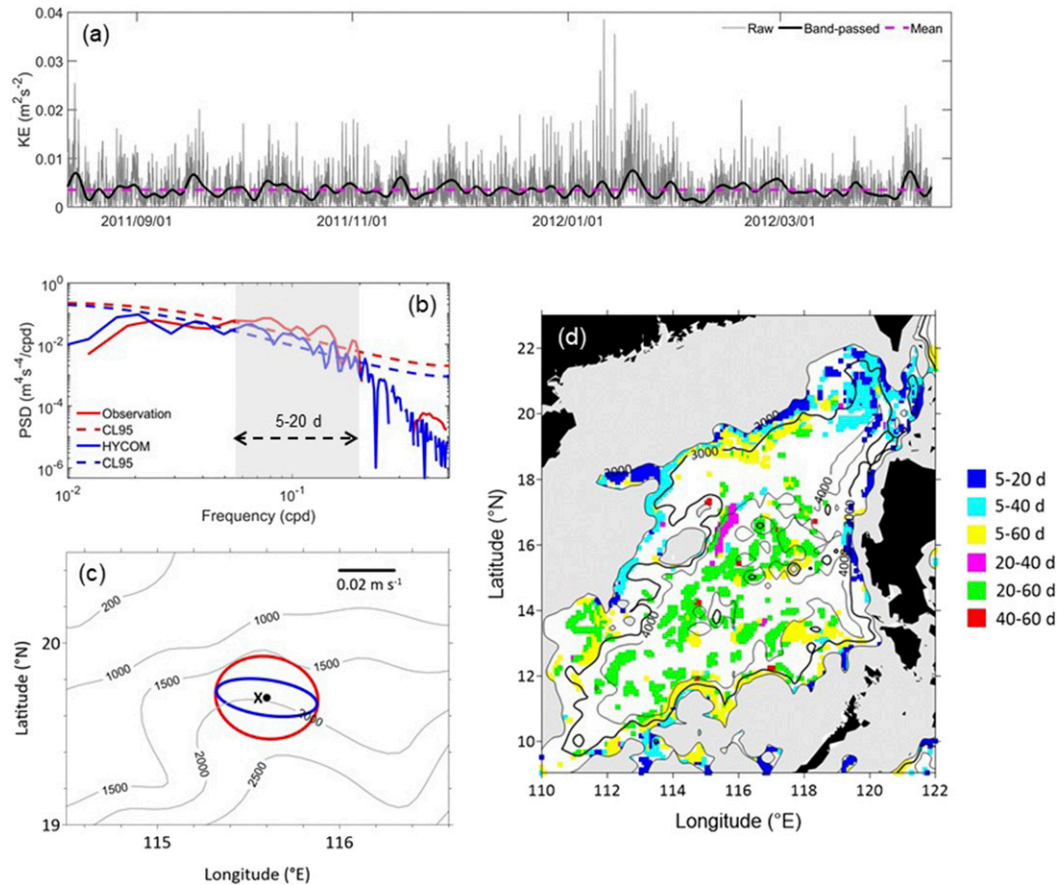
FIG. 4. (a) Time series of the observed bottom KE ($m^2\,s^{-2}$) at site X for raw (thin gray line) and 5–90-day bandpassed (thick black line) data. (b) Power spectra of 5–90-day bandpassed bottom KE at site X for observations (red solid line) and HYCOM data (blue solid line). The significant components over the 95% confidence level are shaded. (c) STD ellipses of 5–20-day bandpassed bottom velocity at site X for observations (red) and HYCOM data (blue). Contours denote the isobaths. (d) Significant period bands (days) of the depth-integrated KE below 2000 m in the deep SCS at the 95% confidence level from HYCOM data. Black lines denote the isobaths. The white space means that there is no significant variability of deep-layer KE at the 95% confidence level falling in the intraseasonal time scale (5–90 days) at these locations.

major axis but a shorter minor axis (blue ellipse in Fig. 4c). It implies that the modeled fluctuations are close to the observations in strength but more rectilinear. In spite of some uncertainties, HYCOM GLBv0.08 is believed to be feasible for our study and hence is employed for the following analysis.

To determine the dominant time scales of the deep-flow variability in the entire SCS, we conduct power spectrum analysis of the depth-integrated KE below 2000 m. Most of the spectra meeting the 95% confidence level fall in the intraseasonal time scale (5–90 days) and are concentrated over sloping topography (Fig. 4d). The significant periods typically range from 5 to 60 days, but individual bands (bounded by the local minimum and maximum periods) vary spatially. In the eastern, northeastern, and northwestern regions of the basin, the frequencies are relatively high, and the bands are narrower, namely, 5–20 and 5–40 days. In the northern and southern slope regions, the frequencies decrease offshore, and the bands tend to be broader (from 5–20 to 5–60 days). In the DWBC and

central seamount regions, the frequencies are relatively low, and most of the bands are 20–60 days.

A comparison of Fig. 4d with the distributions of the smoothed topographic gradient ($|\nabla h|$, Fig. 5a) and the 6-yr-mean Brunt–Väisälä frequency averaged over the bottom 200 m (N, Fig. 5b) in the deep SCS reveals that the periods tend to be shorter for steeper topography and stronger stratification, and vice versa. The relationships between the significant periods and the environmental parameters (i.e., $|\nabla h|$ and N) show some typical characteristics of TRWs if Eq. (6) is considered. Figure 5c exhibits the theoretical minimum period $P_{\min} = 2\pi/(N|\nabla h|)$ allowed by the TRW dispersion relation. In the interior basin where both $|\nabla h|$ and N are small, $P_{\min}$ can even reach 60 days or longer. However, such theoretical long-period TRWs probably do not exist in the present model because there is no significant variability of deep-layer KE at the 95% confidence level falling in the intraseasonal time scale (<90 days) at these locations (see the white space in Fig. 4d).
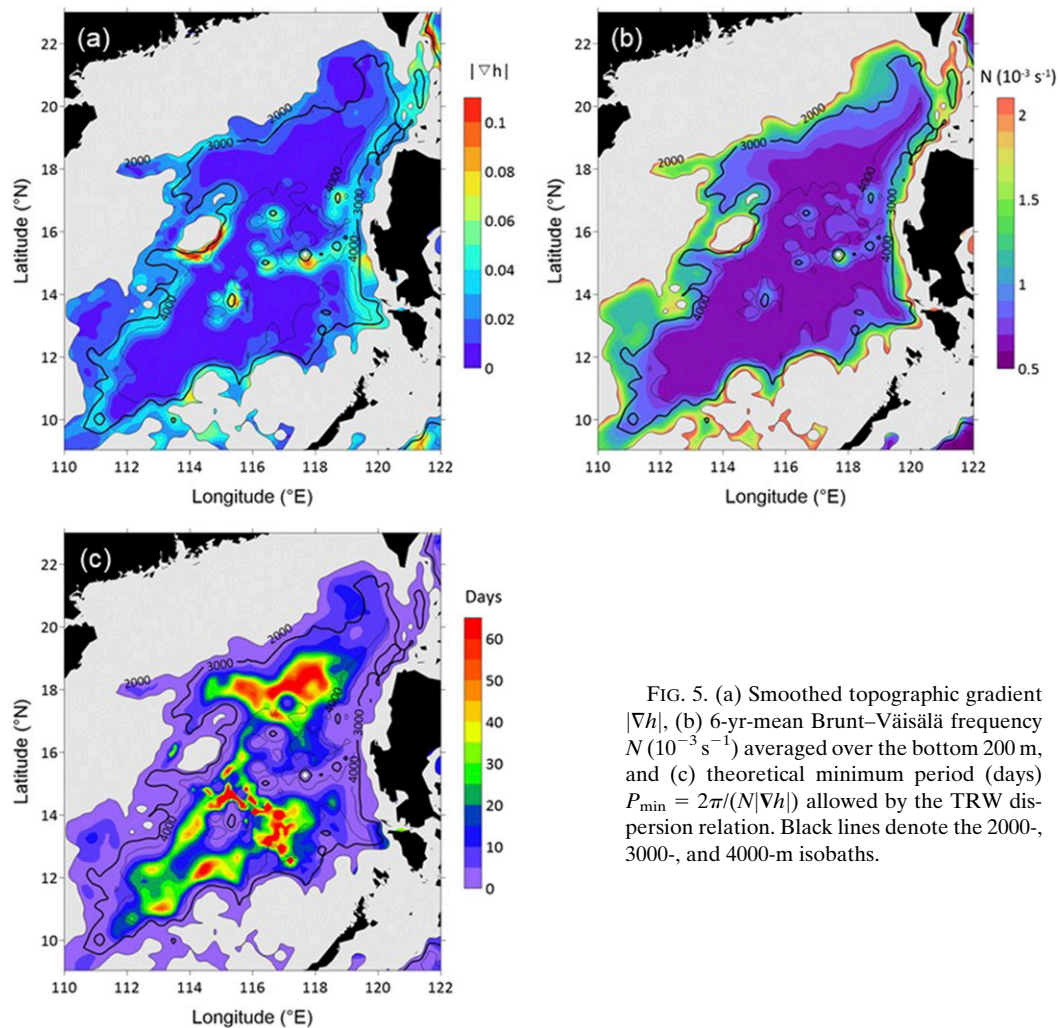
FIG. 5. (a) Smoothed topographic gradient $|\nabla h|$, (b) 6-yr-mean Brunt–Väisälä frequency $N (10^{-3} \, \text{s}^{-1})$ averaged over the bottom 200 m, and (c) theoretical minimum period (days) $P_{\min} = 2\pi/(N|\nabla h|)$ allowed by the TRW dispersion relation. Black lines denote the 2000-, 3000-, and 4000-m isobaths.

In the eastern, northeastern, and northwestern areas of the basin, both $|\nabla h|$ and N are large. The theoretical minimum period $P_{\min}$ in these regions is generally shorter than 20 days, suggesting that high-frequency TRWs can be supported. As a result, the maximum periods in Fig. 4d are shorter than 40 days in these regions. By contrast, in the DWBC and central seamount regions, although $|\nabla h|$ is large, the stratification is weak. Consequently, we have $P_{\min} \geq$ 20 days or longer in these regions. Hence, the short-period ($<$20 days) fluctuations in Fig. 4d almost disappear. In the northern and southern slope regions, where $|\nabla h|$ and N decrease gradually offshore, $P_{\min}$ as well as the maximum periods in Fig. 4d tend to be longer seaward. These environmentally dependent features suggest that the deep SCS intrinsically favors these periodic fluctuations. To further identify the TRWs from these intraseasonal fluctuations, more wave-related features must be examined.

c. Spatiotemporal structure

According to Thompson and Luyten (1976), the angle θ in Eq. (6) is also the angle between the velocity vector and the isobaths, which can be simplified under the assumptions $\tanh(\lambda_r h) \approx 1$ and $\beta = 0$ to

$$\theta = \sin^{-1} \left(\frac{\omega}{N|\nabla h|} \right). \tag{9}$$

Thus, the major principal axis of the STD ellipse of the velocity at low frequency is expected to be parallel to the local isobath. Observations and model results at site X have revealed this kind of phenomenon (Fig. 4c). To further examine whether the intraseasonal fluctuations in other regions of the deep SCS have these typical characteristics of TRWs, we select a series of locations along the 3000-m isobath (Fig. 6) and apply a band-pass filter to the horizontal velocities to examine the spatiotemporal structure of the deep flow at these locations. Most of the STD ellipses of the bandpassed velocities in Fig. 6 are flat, and the major principal axes are parallel to the local isobath, indicating that the currents change by flowing back and forth along the local isobaths. According to Eq. (9), it suggests that the low-frequency components are dominant in the local KE spectra. In addition, the STD ellipse becomes more rectilinear when the topographic beta, $\beta_{\text{top}} = f|\nabla h|/h$, is much stronger
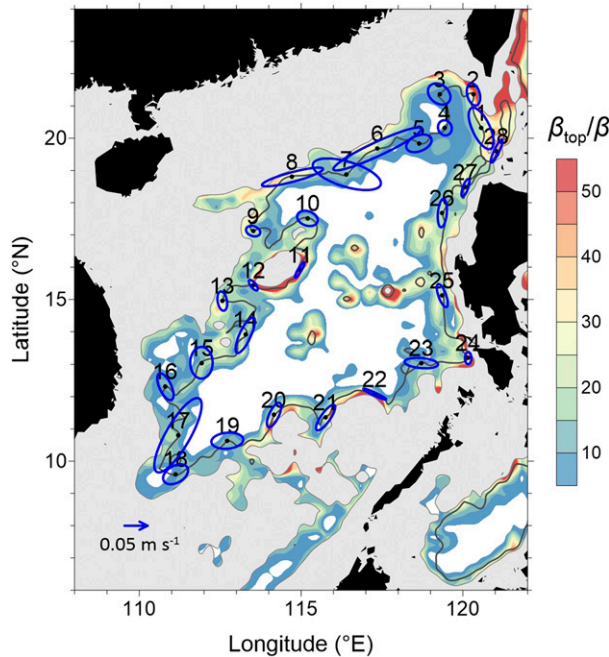
FIG. 6. STD ellipses of velocities at 3000 m filtered within the local period band at the locations numbered cyclonically from 1 to 28. Contours denote the ratio between the topographic beta β_{top} and the planetary beta β. The gray line represents the 3000-m isobath. Areas shallower than 2000 m are masked, and the white space indicates the location where the ratio β_{top}/β is smaller than 5.
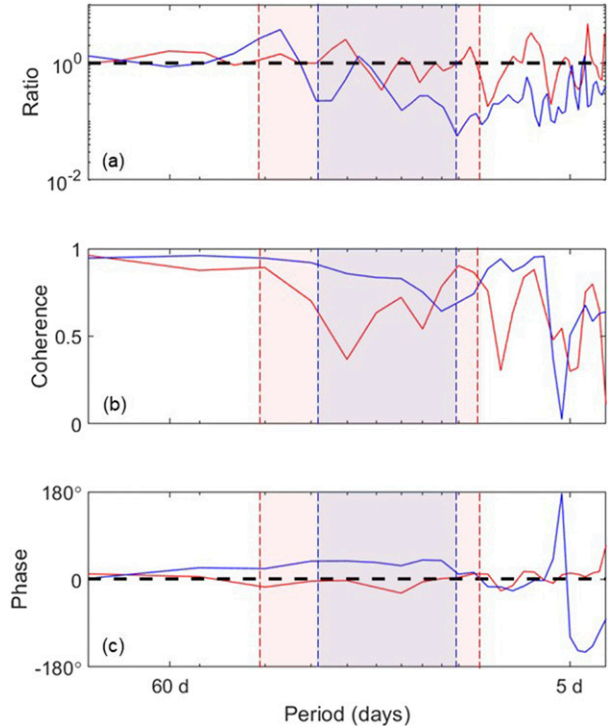

FIG. 7. (a) Ratio, (b) coherence, and (c) phase lag of the KE spectra between 2500 and 3000 m at location 6 (blue line) and location 20 (red line) in Fig. 6. The significant period bands of the KE at the 95% confidence level are shaded.

than the planetary beta β. Consequently, fluctuations are more easily trapped by the topography and hence show a stronger directivity in these regions. These features are quite similar to those observed in TRWs in the deep Gulf of Mexico (Hamilton 2009).

Furthermore, regardless of viscous effect, the amplitude of the TRW-induced horizontal velocity can be expressed as

$$V(z) = V_0 \cosh(\lambda_\nu z), \tag{10}$$

where V_0 is a constant. Equation (10) shows that the velocity should be bottom-intensified within the trapping scale λ_ν^{-1}. Moreover, according to Eq. (6), the phase of the velocity, $\phi = kx + ly - \omega t$, in the water column is coherent if the buoyancy frequency N is constant or a weak function of depth. To illustrate this spatiotemporal structure, we take the results from locations 6 and 20 in Fig. 6 as an example. Figure 7a shows the ratios of the KE spectra between 2500 and 3000 m. Within the significant period bands at the 95% confidence level (shaded), the ratios are mostly less than 1 at both sites, indicating that the currents intensify toward the bottom at the frequencies of interest. Moreover, the variation of the KE at each depth shows high coherence with a small phase lag (Figs. 7b,c). In the region where the planetary beta β is much less than the topographic beta, $\beta_{top} = f|\nabla h|/h$, Eq. (5) can be simplified as $\lambda_\nu^{-1} = f/(NK)$. The trapping scale is then proportional to the Coriolis parameter f but inversely proportional to the buoyancy frequency N for a given wavenumber. It may explain why location 6 has a

larger trapping scale (equivalently, higher coherence in the vertical direction) than location 20, because location 6 has a larger f but a smaller N (Fig. 5b). In addition, the maximum velocities induced by the fluctuations at both locations can reach approximately 0.1 m s^{-1} (not shown), which is one order of magnitude larger than the ambient deep flow in Fig. 3 and close to observations in the northern and southern SCS (Shu et al. 2016; Wang et al. 2019). These spatiotemporal features of the deep flow provide more evidence for TRW identification in the abyssal SCS.

d. Dispersion relation

As a final validation, we examine the dispersion relation of these intraseasonal fluctuations. Because the deep currents at different depths are almost in phase, the ratio of the KE at a given frequency between any two levels should be constant:

$$R = \left(\frac{\cosh\lambda_\nu z_1}{\cosh\lambda_\nu z_2}\right)^2. \tag{11}$$

Equation (11) enables energy-weighted estimation of the vertical trapping scale λ_ν^{-1} of the TRWs at each frequency, which can be used to calculate the magnitude of the wavenumber using the relation $K = f\lambda_\nu/N$ (Thompson and Luyten 1976; Hogg 2000). Assuming that these energetic intraseasonal fluctuations are dominated by the TRWs, we use the KE spectrum at each significant frequency to calculate the ratio R
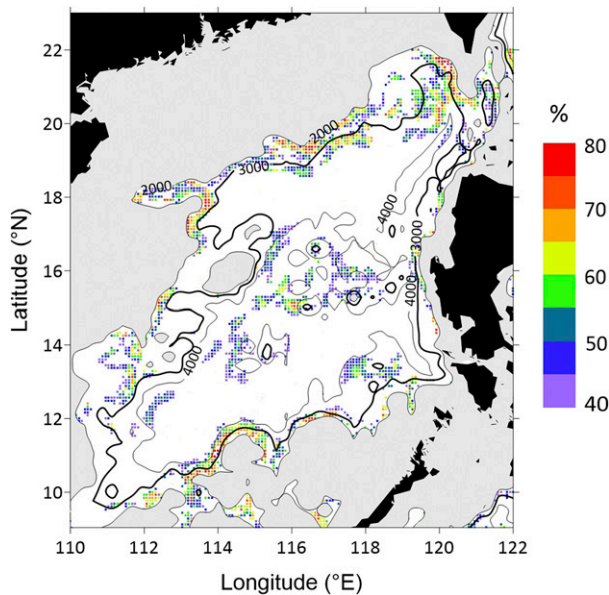
FIG. 8. Ratio between the STD of the bandpassed deep KE (filtered within the individual band at each location in Fig. 4d) and the STD of the total deep KE (integrated from 2000 m to the bottom) at locations where TRWs are identified.

between 2000 and 2500 m, and then solve Eq. (11) to obtain the corresponding trapping scale λ_ν^{-1} and the magnitude of the wavenumber K. For a given wavenumber, we replace θ in Eq. (6) with values ranging from 0 to π to obtain all the possible theoretical ω values and calculate the corresponding 95% confidence intervals (CIs). We then compare the significant frequencies from the spectral analysis in Fig. 4d with the theoretical ω values. Only the results that lie in the 95% CI of the theoretical solutions are considered to be the most typical TRWs.

The results indicate that more than half of the locations in Fig. 4d are valid (Fig. 8), where the ratios between the STD of the bandpassed deep KE (filtered within the individual band at each location in Fig. 4d) and the STD of the total deep KE (integrated from 2000 m to the bottom) exceed 40% in the DWBC and central seamount regions, and even reach 70% over slopes in the northern and southern SCS. This result suggests that the TRWs are energetic and contribute greatly to the deep-current variability over steep topography in the SCS. These results are consistent with the observations at site X and the findings of Hamilton (2009), who found that the TRWs at 10–100 days can account for more than 80% of the total variance of the deep flow in the Gulf of Mexico. According to the energy-weighted estimates, the trapping scales generally range from hundreds to thousands of meters at different frequencies in the deep SCS, and the corresponding wavelengths range from 100 to 500 km (not shown). Note that wavelengths shorter than 100 km are barely resolved by the model owing to the limited resolution. Therefore, the highly bottom-trapped TRWs at short wavelengths are not discussed in this paper.

To illustrate the dispersion diagrams of TRWs in different regions of the deep SCS, the results from six representative
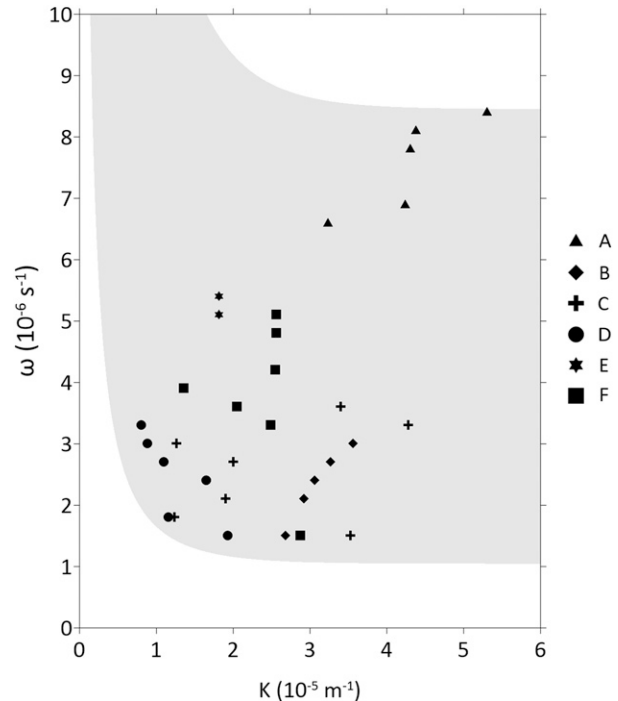

FIG. 9. Dispersion diagrams of TRWs at six representative sites shown in Fig. 10. For the typical environmental parameters $|\nabla h| = 0.02$, $N = 1 \times 10^{-3}\,\mathrm{s}^{-1}$, $f = 4 \times 10^{-5}\,\mathrm{s}^{-1}$, and $h = 3000$ m in the deep SCS, the shaded area denotes the theoretical range of the TRW dispersion relation based on Eqs. (5) and (6) for θ values of 5°–30°.

sites are shown in Fig. 9. As shown in Fig. 10, the sites are located over the slope west of the Luzon Strait (site A; the ratio in Fig. 8 is 64%), southeast of the Dongsha Islands (site B; the ratio is 68%), in the central seamount region (site C; the ratio is 57%), in the DWBC region (site D; the ratio is 45%), north of the Nansha Islands (site E; the ratio is 65%), and west of the Mindoro Strait (site F; the ratio is 49%). At each location, because the environmental parameters h, ∇h, and N exhibit spatial inhomogeneity, the distributions of the wave properties are expected to show anisotropy in geographic space and complicated overlap in wavenumber space (Rhines and Bretherton 1973; Pickart 1995; Oey and Lee 2002; Hamilton 2009). At site A, the TRWs with high frequencies have shorter wavelengths (100–200 km). The TRWs at sites B–F have similar frequencies, but their wavelengths differ greatly. Long wavelengths (300–500 km) appear in the west (site D) and south (site E), whereas intermediate wavelengths (150–300 km) are present in the north (site B). In the central and eastern SCS (sites C and F), the wavelengths show a broad distribution ranging from 150 to 500 km. These results are generally in the theoretical range of the TRW dispersion relation estimated using the typical environmental parameters for the deep SCS.

In this section, we set three constraints to identify the most typical TRWs in the deep SCS. 1) The intraseasonal fluctuations must be significant at the 95% confidence level at each location. This constraint ensures that the KE on the relevant
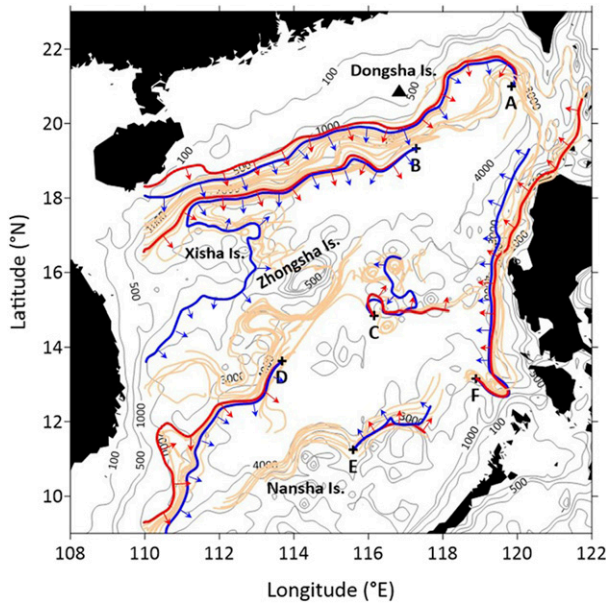
FIG. 10. TRW rays in the deep SCS (light orange lines). Results from site A (9.3 and 11 days), site B (24.2 and 30.3 days), site C (20.2 and 48.4 days), site D (26.9 and 48.4 days), site E (13.4 and 14.2 days), and site F (15.1 and 22 days) are highlighted for analysis. Rays at relatively high (low) frequencies are shown in red (blue). Arrows indicate the directions of the wavenumber vectors. Contours indicate isobaths.

time scale is prominent in the full energy spectrum. 2) The intraseasonal fluctuations must be in phase and bottom intensified. This constraint enables energy-weighted estimation of the vertical trapping scale and wavenumber magnitude. 3) The significant frequency and the corresponding wavenumber must be consistent with the theoretical dispersion relation. Note that these constraints are probably overly restrictive and may eliminate potential sites where TRWs coexist with other strong locally forced intraseasonal components. However, these strict constraints ensure that we consider only robust TRWs that are hardly interfered by other processes and may have a better chance of being observed in the SCS.

4. Propagation of TRWs in the deep SCS

Now that we have revealed the spatiotemporal features of TRWs in the deep SCS, we investigate the wave propagation in this section. First, we trace the TRW rays to obtain various wave properties along their paths, without considering the background flow. Then we integrate the background flow into the model to assess the effects of the basin-scale circulation on wave propagation.

a. Environmental fields

The ray tracing model uses four environmental parameters: N, h, h_x, and h_y. All the parameters are taken from HYCOM GLBv0.08. Under the WKB approximation, these parameters should vary slowly in space and time. Hence, we use the smoothed topography and stratification in the model. Finally, a 2D spline is fitted to the smoothed bathymetry and the

buoyancy frequency so that h, ∇h, and N can be computed at any location in the domain.

b. Initial positions and wavenumber vectors of rays

To trace the TRW rays, the initial position and wavenumber vector, as well as the frequency defined for each ray, should be assigned. The frequencies and wavenumber vectors from the locations that passed the validation in section 3 can be used in the model. To clearly illustrate the wave propagation in different areas of the deep SCS, TRW rays at different frequencies are released at as many locations as possible. Because the wave periods range from 5 to 60 days, the model is integrated forward for 60 days with a time step of 1 h to cover all the possible periods.

c. Results without considering background flow

In this section, we set $\mathbf{v}_h = 0$ in Eqs. (7) and (8) to trace the TRW rays and obtain the wave properties along their paths. Figure 10 shows the TRW rays in the deep SCS (light orange lines); the results from the six representative sites are highlighted for analysis. Note that at each site, the rays at relatively high (low) frequencies appear in red (blue). Similar to results for the Gulf Stream region (Pickart 1995) and the Gulf of Mexico (Oey and Lee 2002; Hamilton 2009), the ray paths extend along the steep topography and are directed upslope with phase propagation offshore. Oey (2008) used an idealized wave–eddy coupling model to interpret the upslope radiation of TRW energy. Inspired by his work, we rewrite Eq. (6) as

$$\tanh(\mu) = S/\mu, \tag{12}$$

where $S = K|\nabla h|\sin(\theta)hN^2/f\omega$, and $\mu = \lambda_r h$. Equation (12) has real solutions for μ only when $S > 0$. Taking the rays emanating from site A as an example, we assume for simplicity that the depth decreases only northward ($\partial h/\partial y < 0$) and the frequency can be written as

$$\omega = lc, \tag{13}$$

where c is the meridional component of the phase velocity. To obtain a positive ω for $f > 0$, $\sin(\theta)$ must be positive (i.e., $0 < \theta < \pi$), which means that the wave propagates with shallower water to the right in the Northern Hemisphere (Fig. 2). Because a smooth basin with weak stratification is a natural boundary for evanescent waves, TRWs can survive only when the wavenumber vectors point seaward ($l < 0$ and $c < 0$) and the energy is radiated upslope (in this case, $0 < \theta < \pi/2$).

According to Eq. (9), because the frequency is constant along each ray path, rays tend to become more aligned with the local isobath as the topography steepens or the stratification becomes stronger. In addition, TRWs at higher frequencies have a larger angle θ for the given environmental parameters. Consequently, for rays at different frequencies released at the same place, the high-frequency rays show a stronger climbing effect that enables them to cross the isobaths, whereas the low-frequency rays tend to veer along the isobaths when they encounter steep topography. This behavior explains why the high-frequency TRW released at site B can propagate continuously westward onto the upper slope, whereas the low-
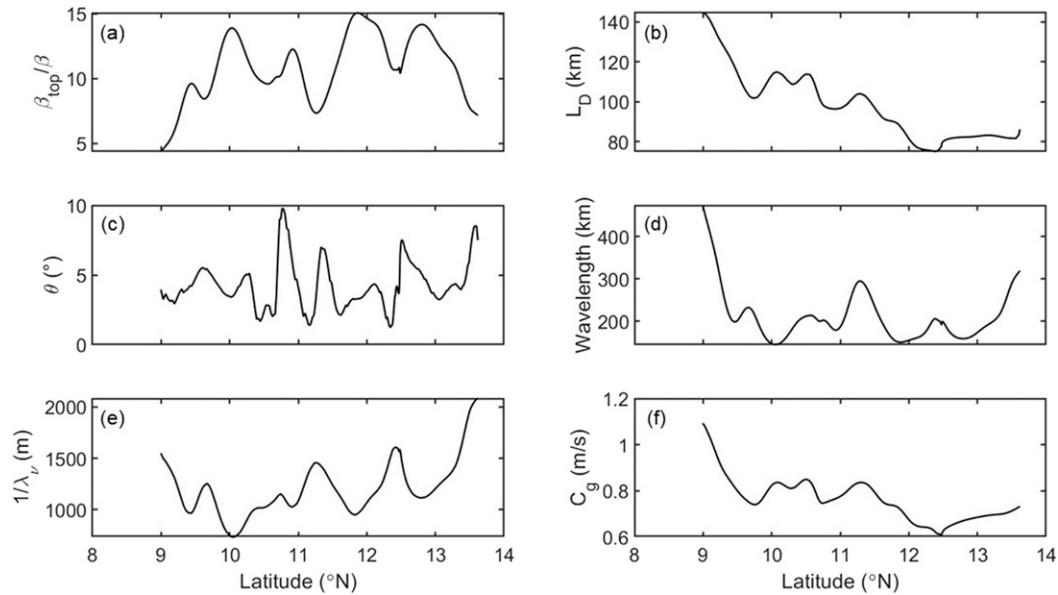
FIG. 11. Properties of the 48.4-day TRW along the ray path (blue line) released at site D in Fig. 10: (a) ratio of β_{top} to β; (b) internal Rossby deformation radius L_D (km); (c) angle θ (°); (d) wavelength (km); (e) trapping scale λ_ν^{-1} (m); (f) group velocity (m s^{-1}).

frequency one must detour around the Xisha Islands. The rays emanating from other sites exhibit similar behavior.

To further explore the variations of wave properties along the ray path, we take the 48.4-day TRW ray released at site D as an example (Fig. 11). In the deep SCS with steep topography, the typical environmental parameters are $N = 1.0 \times 10^{-3}\,\text{s}^{-1}$, $h = 3000\,\text{m}$, $|\nabla h| = 0.02$, and $f = 4 \times 10^{-5}\,\text{s}^{-1}$. Hence, the topographic beta, $\beta_{top} = f|\nabla h|/h = 2.7 \times 10^{-10}\,\text{m}^{-1}\,\text{s}^{-1}$, is one order of magnitude larger than the planetary beta, $\beta = 2.0 \times 10^{-11}\,\text{m}^{-1}\,\text{s}^{-1}$. Moreover, because the estimated wavelengths are shorter than 500 km (i.e., $K \geq 1.26 \times 10^{-5}\,\text{m}^{-1}$), we have $NhK/f \gtrsim 0.942 \approx O(1)$ and $\coth(\lambda_\nu h) \approx 1$. Equations (5) and (6) can be combined and expressed as follows (Pedlosky 2003):

$$\omega = \beta_{top} L_D \sin(\theta), \tag{14}$$

where $L_D = Nh/f$ is the internal Rossby deformation radius. Equation (14) illuminates more clearly the physical meaning of the fact that TRWs depend on the topographic beta β_{top} and are K independent at each frequency, and that the waves are highly bottom trapped when the wavelength is less than L_D.

The ray traverses the topography at a β_{top}-dominated angle θ and terminates early around the tenth day. Because the frequency ($\omega = 1.5 \times 10^{-6}\,\text{s}^{-1}$) is constant along the ray, the ratio β_{top}/β (Fig. 11a) should be greater than 7.5 to sustain the dispersion relation if we use the last values of $L_D = 142\,\text{km}$ and $\sin(4°) = 0.07$ near 9°N (Figs. 11b,c) in the estimation. In fact, the value of β_{top}/β, tends to be less than 5, and the ray terminates, indicating that the topography is too gentle to support TRWs of certain frequencies. The differences in the refraction and termination of TRW rays at different

frequencies in Fig. 10 reflect the environmentally dependent screening processes of the waves in the abyssal SCS.

Along the ray path, the wavelength shows a decrease (14°–12°N)–increase (12°–11°N)–decrease (11°–10°N)–increase (10°–9°N) pattern (Fig. 11d). To examine the factors controlling the wavelength variations, following Oey and Lee (2002), we multiply Eq. (8) by the wavenumber vector **K** and use Eq. (14) to obtain

$$d(K^2/2)/dt = -k\sin(\theta)\partial(L_D\beta_{top})/\partial x, \tag{15}$$

where we assume for simplicity that β_{top} and L_D vary zonally (Fig. 5). Because both k and $\sin(\theta)$ are positive, and L_D tends to increase along the path (Fig. 11b), the wavelength variation is determined largely by β_{top}. As the ray stretches southwestward, β_{top} shows an increase ($\partial\beta_{top}/\partial x < 0$; 14°–12°N)–decrease ($\partial\beta_{top}/\partial x > 0$; 12°–11°N)–increase (11°–10°N)–decrease (10°–9°N) pattern (Fig. 11a), which mirrors the variation of $d(K^2/2)/dt$. Similar results along other ray paths (not shown) reveal that the topographic beta is the dominant contributor to the wavelength variation, which is consistent with studies of the Gulf Stream region and the Gulf of Mexico (Pickart 1995; Oey and Lee 2002).

In contrast to the short wavelengths (e.g., 82 and 13 km) with small trapping scales (325 and 238 m) observed by Shu et al. (2016) and Wang et al. (2019), the modeled TRW wavelength exceeds 150 km and is larger than the deformation radius L_D. Consequently, the wave is weakly bottom trapped; the trapping scale, $\lambda_\nu^{-1} = f/NK$, ranges from 700 to 2000 m (Fig. 11e) and varies consistently with the wavelength. Note that site D is in the DWBC region of the SCS, and the results are comparable to those for the long TRW (130 km at a 40-day period, with a trapping scale of 1700 m)

observed in the DWBC region at Cape Hatteras (Pickart and Watts 1990).

Using Eq. (14), the group velocity $|\mathbf{C}_g| = |\nabla_{\mathbf{K}}\omega|$ can be written as

$$|\mathbf{C}_g| = \beta_{\text{top}} L_D |\cos(\theta)|/K. \tag{16}$$

Unlike the wavelength and trapping scale, which depend strongly on β_{top}, the group velocity (Fig. 11f) seems to be dominated by the variation of the deformation radius L_D. Because long waves are weakly bottom trapped and close to the fast barotropic mode (Wang and Mooers 1976; Olbers et al. 2012), they propagate at an extremely high speed of more than $0.6\,\mathrm{m\,s^{-1}}$, which exceeds the estimated speed of $0.4\,\mathrm{m\,s^{-1}}$ at wavelengths shorter than 60 km in the northern SCS (Wang et al. 2019). According to Eq. (16), the group velocity is proportional to the wavelength for a given β_{top} and L_D. This fact may explain why TRWs with longer wavelengths propagate faster in the DWBC region than in the northern SCS (see the wavenumbers at sites B and D in Fig. 9).

d. Effect of background circulation on TRW rays

To assess the effect of the basin-scale circulation on TRW propagation, we set $\mathbf{v}_h(x, y)$ to the 6-yr-mean velocity averaged over the bottom 200 m from HYCOM GLBv0.08. Figure 12 shows that the wave rays in the northern and western regions of the SCS are almost unaffected by the background circulation. The reason is that the abyssal circulation is slower than $0.1\,\mathrm{m\,s^{-1}}$, so it is much weaker than the group velocity of the TRWs (which is generally greater than $0.2\,\mathrm{m\,s^{-1}}$) in these regions. The background flow affects the rays only when the TRWs reach the upper slope ($<$500 m), where the velocity of the northern branch of the upper-layer circulation is comparable to the group velocity (see the rays emanating from site A). By contrast, in the central, southern, and eastern SCS, where the group velocities are approximately $0.1\,\mathrm{m\,s^{-1}}$, the wave rays are more sensitive to the background flow. Because the group velocities are oriented in essentially the same direction as the background flow, the propagation speed is greater, and the rays can extend for longer distances, according to Eq. (7), as long as the environment can sustain the dispersion relation for a given frequency. Taking the ray released at site F as an example, Eq. (15) can be rewritten as

$$d(K^2/2)/dt = -k\sin(\theta)\partial(\beta_{\text{top}} L_D)/\partial x - kl\partial v/\partial x. \tag{17}$$

Because k is negative and $\partial v/\partial x$ is positive along the ray, the background circulation with horizontal shear can increase (decrease) the wavelength when $l < 0$ ($l > 0$). Moreover, the absolute frequency ω_a is related to Eq. (14) by the Doppler relation as

$$\omega_a = \beta_{\text{top}} L_D \sin(\theta) + |\mathbf{v}_h| K \cos(\varphi), \tag{18}$$

where φ is the angle between the background flow and the wavenumber vector. Because ω_a is constant along the ray, the ray path tends to turn downslope (upslope) when the background flow is more aligned with (deviates from) the wavenumber vector.
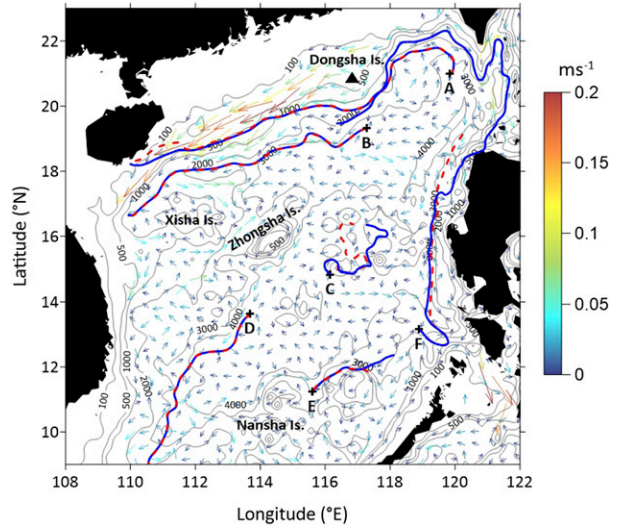

FIG. 12. TRW rays with (blue solid lines) and without (red dashed lines) considering the background flow, released at site A (9.3 days), site B (24.2 days), site C (48.4 days), site D (48.4 days), site E (13.4 days), and site F (22 days). Colored arrows indicate the 6-yr-mean currents averaged over the bottom 200 m. Contours indicate isobaths.

These results indicate that background flow with horizontal shear can affect the properties (e.g., group speed, wavelength, and direction) of TRWs during propagation if the flow velocity is comparable to the group velocity. The group velocity of TRWs is proportional to the wavelength for given environmental parameters (i.e., N, h, and ∇h). Note that the wavelengths estimated from HYCOM GLBv0.08 are longer than 100 km. The unresolved short-wavelength ($<$100 km) TRWs in the abyssal SCS are likely to be more sensitive to the background circulation.

5. Discussion

Following studies of the Gulf of Mexico (Oey and Lee 2002; Hamilton 2009), we use a specific event as an example to illustrate the possible sources of TRW energy in the abyssal SCS. On the basis of the results in section 3, we employ multiscale energy and vorticity analysis (MS-EVA; Liang and Anderson 2007; Liang 2016) to separate the original data into three scale windows: the nonstationary background flow window ($>$64 days; $\varpi = 0$), the mesoscale fluctuation window (8–64 days; $\varpi = 1$), and the high-frequency fluctuation window ($<$8 days; $\varpi = 2$). Note that the window bounds are exponential functions of base 2 for the MS-EVA. We then examine the terms in Eqs. (A13) and (A14) in each window to determine the intra and interscale energetics of the deep SCS. The MS-EVA procedure is described in detail in the appendix. The results from the window $\varpi = 1$ (variables with superscript "1") include information on TRWs and thus are selected for analysis.

Most of the previous studies tended to attribute the energy source of TRWs to the mesoscale perturbations (e.g., eddies) in
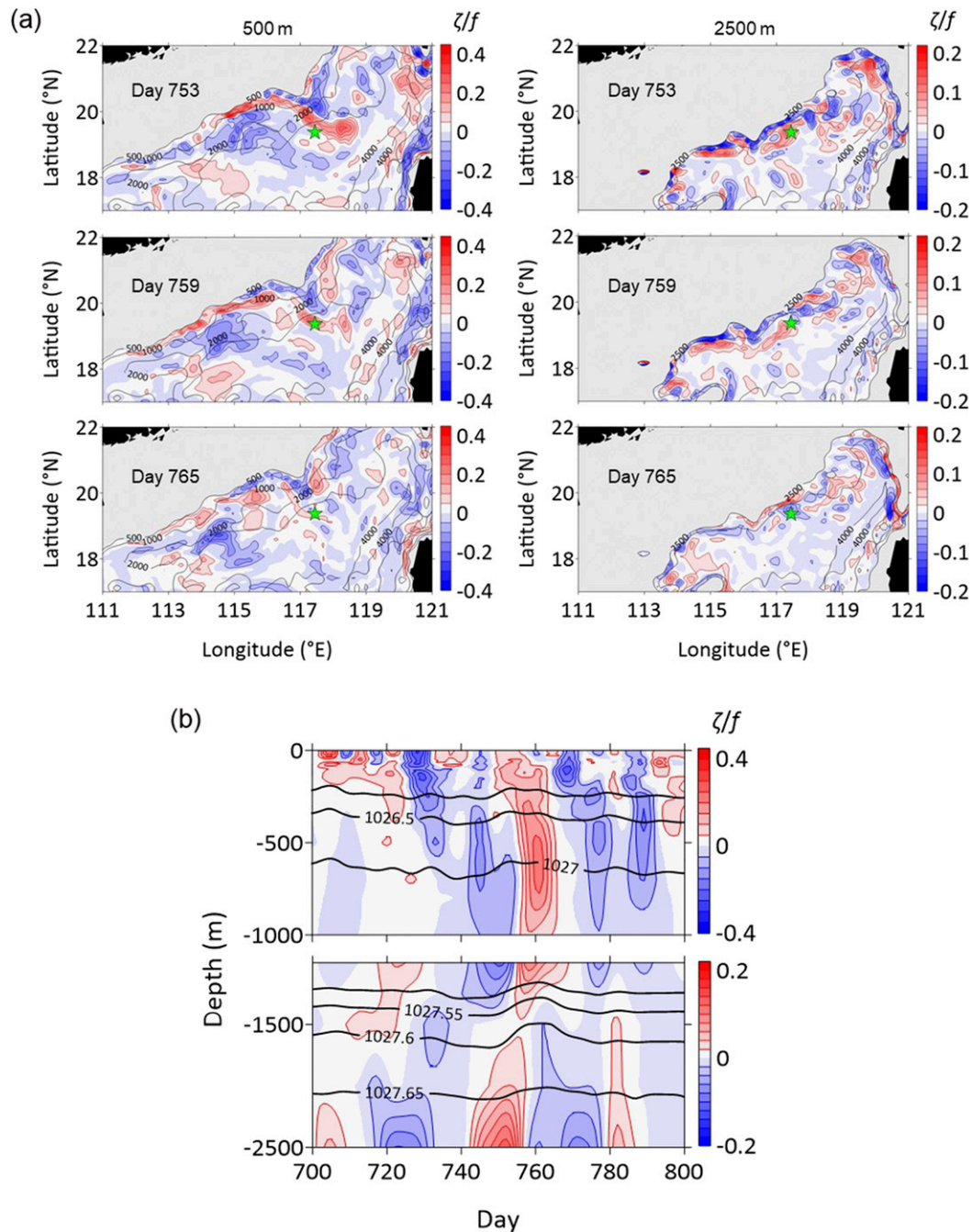
FIG. 13. (a) Horizontal maps of the relative vorticity ζ^1 (as a fraction of f) at (left) 500 and (right) 2500 m in the northern SCS on days 753 to 765. The green star indicates site B in Fig. 10. (b) Profile of the relative vorticity ζ^1 (as a fraction of f) at site B. Black contours indicate the isopycnals (kg m^{-3}).

the upper layer (Hamilton 2009; Shu et al. 2016; Ma et al. 2019; Wang et al. 2019). To reflect the wave pattern and the interactions of the mesoscale motions between layers, we use the filtered vorticity from the window $\varpi = 1$ for illustration. In addition, to exhibit the robust TRWs and the related energetics without the interferences from other strong locally forced non-TRW components, we take site B in Fig. 10 where the TRWs

have been identified under the strict constraints as a representative station for analysis. Because TRWs seem to be most active in the slope region of the northern SCS (Fig. 8), Fig. 13a shows horizontal maps of the relative vorticity ζ^1 (as a fraction of f) at 500 and 2500 m in the northern SCS at a 6-day interval from day 753 to day 765 (note that we use day numbers in this study for convenience). Within this period, a strong
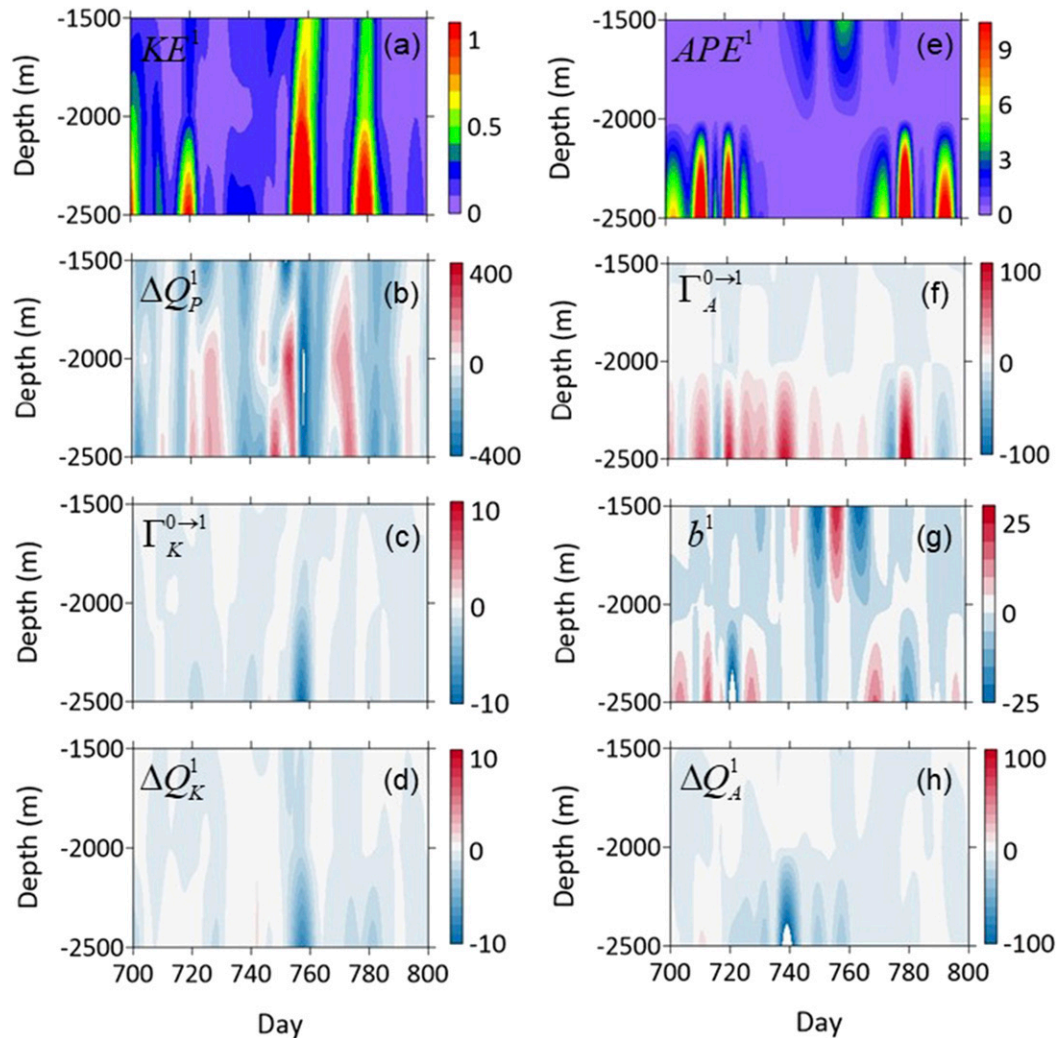
FIG. 14. Profiles of the energy reservoir (J m^{-3}) and energetics (10^{-6} W m^{-3}) for (left) KE^1 and (right) APE^1 at site B.

perturbation with positive ζ^1 sweeps over site B (indicated by the green star) at 500 m. After a slight lag, negative ζ^1 appears at site B in the deep layer and merges into the alternating cyclonic–anticyclonic meanders along the slope. To further illustrate the relationship between the upper and deep layers during this period, we analyze the evolution of the relative vorticity throughout the water column at site B (Fig. 13b). Wavelike fluctuations are clearly present below 2000 m, and the deep relative vorticity is opposite to that above. From a depth-integration viewpoint, this opposite vertical pattern indicates the process of PV adjustment to the changing depth of the interface between layers (see the variation of the isopycnals). When strong perturbations with positive/negative ζ^1 sweep over from above, the isopycnals are strongly deformed, and the deep vorticities become stronger. This phenomenon is most apparent in the event on days 753–765, in which an intense perturbation passes by and cause a dramatic rise of the isopycnals. Because the deep intraseasonal fluctuations at site B were identified as TRWs in section 3, the generation and intensification of the waves are believed to be closely associated with mesoscale perturbations in the upper layer. This is consistent with observations in the SCS and Gulf of Mexico (Shu et al. 2016; Wang et al. 2019; Hamilton 2009).

To more thoroughly examine the dynamics of how the deep fluctuations are excited or intensified, Fig. 14 shows the energy reservoir and energetics in the deep layer at site B (note that the implicit F terms and negligible transfer terms $\Gamma^{2\to1}$ are not shown). The largest KE^1 bursts appear in the event on days 753–765. During this event, the positive pressure work ΔQ_P^1 resulting from the tilted isopycnals is the dominant contributor to the increase in KE^1, whereas the negative transfer $\Gamma_K^{0\to1}$ causes an inverse energy cascade from KE^1 to KE^0. The negative transport ΔQ_K^1 tends to carry KE^1 away. This result suggests that intense perturbations from above can fuel energy into the deep fluctuations by distorting the isopycnals to do work, and some of the gained KE^1 is transferred upscale to the

TABLE A1. Expressions and physical meanings of each term in Eqs. (A13) and (A14) on window ϖ. Note that the colon operator is defined such that, for two dyadic products $\mathbf{AB}$ and $\mathbf{CD}$, $(\mathbf{AB}):(\mathbf{CD}) = (\mathbf{A} \cdot \mathbf{C})(\mathbf{B} \cdot \mathbf{D})$.

KE^{ϖ}	$\dfrac{1}{2}\hat{\tilde{\mathbf{v}}}_h^{\varpi} \cdot \hat{\tilde{\mathbf{v}}}_h^{\varpi}$	KE on window ϖ
$-\nabla \cdot \mathbf{Q}_K^{\varpi}$	$-\nabla \cdot \left[\dfrac{1}{2}(\widehat{\mathbf{v}\mathbf{v}_h})^{\sim\varpi} \cdot \hat{\tilde{\mathbf{v}}}_h^{\varpi} \right]$	Transport of KE on window ϖ
Γ_K^{ϖ}	$\dfrac{1}{2}[(\widehat{\mathbf{v}\mathbf{v}_h})^{\sim\varpi}:\nabla\hat{\tilde{\mathbf{v}}}_h^{\varpi} - \nabla \cdot (\widehat{\mathbf{v}\mathbf{v}_h})^{\sim\varpi} \cdot \hat{\tilde{\mathbf{v}}}_h^{\varpi}]$	Canonical transfer of KE to window ϖ
$-\nabla \cdot \mathbf{Q}_P^{\varpi}$	$-\nabla \cdot \left(\dfrac{1}{\rho_0}\hat{\tilde{\mathbf{v}}}^{\varpi}\hat{P}^{\sim\varpi} \right)$	Pressure work on window ϖ
b^{ϖ}	$\dfrac{g}{\rho_0}\hat{\rho}^{\sim\varpi}\hat{w}^{\sim\varpi}$	Buoyancy conversion on window ϖ
APE^{ϖ}	$\dfrac{1}{2}c\,(\hat{\rho}^{\sim\varpi})^2, \quad c = \dfrac{g^2}{\rho_0^2 N^2}$	APE on window ϖ
$-\nabla \cdot \mathbf{Q}_A^{\varpi}$	$-\nabla \cdot \left[\dfrac{1}{2}c\hat{\rho}^{\sim\varpi}(\widehat{\mathbf{v}\rho})^{\sim\varpi} \right]$	Transport of APE on window ϖ
Γ_A^{ϖ}	$\dfrac{c}{2}[(\widehat{\mathbf{v}\rho})^{\sim\varpi} \cdot \nabla\hat{\rho}^{\sim\varpi} - \hat{\rho}^{\sim\varpi}\nabla \cdot (\widehat{\mathbf{v}\rho})^{\sim\varpi}]$	Canonical transfer of APE to window ϖ
S_A^{ϖ}	$\dfrac{1}{2}\dfrac{\partial c}{\partial z}\hat{\rho}^{\sim\varpi}(\widehat{\rho w})^{\sim\varpi}$	Apparent source/sink of A^{ϖ} due to the nonlinearity of the reference stratification (usually negligible)

background flow or redistributed by transport. In addition, in the variation of APE^1, positive transfer $\Gamma_A^{0\to1}$ from APE^0 to APE^1 occurs frequently in the deep layer and is usually followed by negative buoyancy conversion b^1 and negative transport ΔQ_A^1. This finding suggests another way that energy is injected into the TRWs; specifically, the deep background flow tends to transfer APE^0 to APE^1 through baroclinic instability, and then part of APE^1 can be converted to KE^1 (i.e., the baroclinic energy pathway, $\mathrm{APE}^0 \to \mathrm{APE}^1 \to \mathrm{KE}^1$) or carried away by advection. Note that

this process appears to occur at locations where the topographic gradient is not too large (not shown). This result might be explained by the previous study (LaCasce 1998; LaCasce et al. 2019) that baroclinic instability is effectively suppressed when the topography is too steep.

The results from site B illustrate two possible sources of TRW energy: mesoscale perturbation in the upper layer and large-scale background flow in the deep layer. The former provides KE by deforming the isopycnals to do work (i.e., pressure work), whereas the latter transfers the APE by
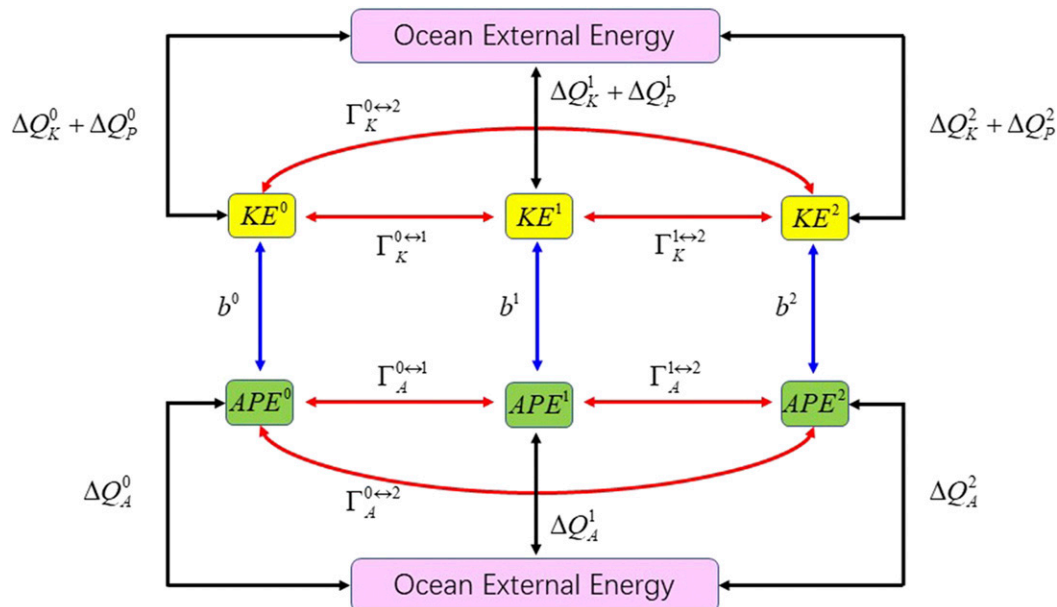

FIG. A1. Energy cycle diagram for the local ocean domain in a three-window framework. Red, blue, and black arrows indicate canonical transfer between different scale windows, buoyancy conversion connecting the KE and APE reservoirs, and advective transport, respectively. Note that the forcing/dissipation processes in each window are not shown.

baroclinic instability (i.e., baroclinic transfer). It seems to be a frequent forcing problem rather than an individual response because Wang et al. (2019) used observations to show numerous mesoscale eddies crossing the area of concern and supporting the deep fluctuations, which are also well reproduced in the data we used (not shown). This result is similar to the findings in the Gulf of Mexico that the deep-layer energy on the mesoscale window comes primarily from the upper layer via pressure work and secondarily from baroclinic instability in the deep layer (Yang et al. 2020; Maslo et al. 2020). More details about the basinwide energetics of the abyssal SCS for the entire intraseasonal regime (8–128 days) can be referred to our recent study (ready for submission).

6. Summary

TRWs in the abyssal SCS were investigated using observations and high-resolution reanalysis data. These energetic waves can account for more than 40% of the deep KE variability in the DWBC and central seamount regions, and this proportion can even reach 70% over slopes in the northern and southern SCS. The wave-induced flow shows columnar (i.e., in phase) structure in which the speed increases toward the bottom. Most of the major principal axes of the corresponding STD ellipses are parallel to the local isobaths, suggesting that the low-frequency components are predominant in the TRW-related spectra. Wave properties such as the period (5–60 days), wavelength (100–500 km), and trapping scale (10^2–10^3 m) depend strongly on the environmental parameters of the SCS, including the stratification, water depth, and topographic gradient, and hence show significant spatial variation.

A ray tracing model indicated that the TRW energy propagates along the steep topography and is directed upslope with phase propagation offshore. High-frequency TRWs exhibit a stronger climbing effect than low-frequency ones and hence can move further onto the upper slope. For TRW with a certain frequency, the variations of the wavelength and trapping scale are dominated by the topographic beta β_{top}, whereas the group velocity is more sensitive to the internal Rossby deformation radius L_D. Moreover, background circulation with horizontal shear can affect the wavelength and direction of TRWs during propagation if the flow velocity is comparable to the group velocity, particularly in the central, southern, and eastern SCS. The differences in the refraction and termination of TRW rays at different frequencies suggest the presence of environmentally dependent screening processes of the waves in the abyssal SCS.

A case study shows that the robust mesoscale perturbation with positive/negative relative vorticity in the upper layer can distort the isopycnals and excite an opposite vorticity in the deep layer owing to PV adjustment to the changing depth of the interface between layers. During this process, a perturbation from above injects energy into the deep layer by pressure work to excite or intensify TRWs. In addition, the large-scale background circulation in the deep layer tends to transfer the APE to the TRWs through baroclinic instability. Note that this process seems to occur at locations where the topography is not steep enough to suppress the baroclinic instability.

Our aim in this study was to reveal a comprehensive dynamic picture of TRWs against the background of the unique SCS circulation. However, owing to the limited model resolution, waves with short wavelengths (<100 km), which might interact more strongly with the circulation, are not discussed in this paper. Observations and numerical models with higher resolution will be used in our future studies to obtain the full TRW-related spectra and achieve better understanding of the characteristics and dynamics of TRWs and their roles in the multiscale energetics of the abyssal SCS.

Data availability statement. The mooring data are available at https://doi.org/10.6084/m9.figshare.13525838. The HYCOM data can be accessed from https://www.hycom.org/dataserver/gofs-3pt1/analysis.

APPENDIX

Multiscale Energy and Vorticity Analysis in a Three-Window Framework

In this study, we adopt MS-EVA (Liang 2016) to investigate the energy sources of TRWs in the abyssal SCS. MS-EVA is based on a functional analysis tool, that is, the multiscale window transform (MWT; Liang and Anderson 2007), to decompose a function space into a direct sum of several orthogonal subspaces, each with an exclusive time scale. In a three-window framework (i.e., $\varpi = 0, 1, 2$), for a given time series $R(t)$, it can be decomposed via the MWT as

$$R^{\sim 0}(t) = \sum_{n=0}^{2^{j_0}l-1} \hat{R}_n^{j_0} \phi_n^{j_0}(t), \tag{A1}$$

$$R^{\sim 1}(t) = \sum_{n=0}^{2^{j_1}l-1} \hat{R}_n^{j_1} \phi_n^{j_1}(t) - R^{\sim 0}(t), \quad \text{and} \tag{A2}$$

$$R^{\sim 2}(t) = R(t) - R^{\sim 0}(t) - R^{\sim 1}(t), \tag{A3}$$

where $\phi(t)$ is a scaling function constructed by Liang and Anderson (2007) and written as

$$\phi_n^j(t) = \sum_{q=-\infty}^{+\infty} 2^{j/2} \phi[2^j(t+lq)-n+1/2], \quad n = 0, 1, \ldots, 2^j l - 1, \tag{A4}$$

and $\hat{R}_n^{\sim\varpi}$ is the MWT coefficient:

$$\hat{R}_n^{\sim\varpi} = \int_0^l R^{\sim\varpi}(t)\phi_n^{j_2}(t)\,dt. \tag{A5}$$

Here $l = 1$ and $l = 2$ correspond to the periodic and symmetric extension schemes, respectively, and j ($j_0 < j_1 < j_2$) is the scale level. Liang and Anderson (2007) confirmed that there always exists a scale level j_2 such that all the atmospheric/oceanic signals of concern lie in a Hilbert space $V_{l,j} \subset L_2[0, 1]$ generated by the basis $\{\phi_n{}^j(t)\}_{n=0,1,...,2^j l-1}$. Equation (A5) is called the MWT. Using this MWT, Eqs. (A1)–(A3) can be combined as

$$R^{\sim\varpi}(t) = \sum_{n=0}^{2^{j_2}l-1} \hat{R}_n^{\sim\varpi}\phi_n^{j_2}(t), \quad \varpi = 0, 1, 2. \tag{A6}$$

Equations (A5) and (A6) form the transform–reconstruction pair for the MWT.

The primitive governing equations of a hydrostatic and Boussinesq fluid are

$$\frac{\partial \mathbf{v}_h}{\partial t} + \mathbf{v} \cdot \nabla \mathbf{v}_h + f\mathbf{k} \times \mathbf{v}_h = -\frac{1}{\rho_0}\nabla_h P + F_m, \tag{A7}$$

$$\frac{\partial P}{\partial z} = -\rho g, \tag{A8}$$

$$\nabla \cdot \mathbf{v} = 0, \quad \text{and} \tag{A9}$$

$$\frac{\partial \rho}{\partial t} + \mathbf{v} \cdot \nabla \rho = \frac{\rho_0 N^2}{g}w + F_\rho, \tag{A10}$$

where $\mathbf{v}$ is the 3D velocity vector (the subscript h denotes the horizontal component), f is the Coriolis parameter, and g is the gravitational acceleration. The effects of forcing and dissipation are expressed implicitly by the F terms. Note that ρ is the density anomaly from a reference state $\rho_r(z)$, which is the time- and area-mean density, and P is the dynamic pressure related to ρ. The variable N is the Brunt–Väisälä frequency, which is given by $N^2 = -(g/\rho_0)\partial\rho_r/\partial z$; $\rho_0 = 1025\,\mathrm{kg\,m^{-3}}$ is the reference density of seawater.

On the basis of the MWT, the KE and APE in scale window ϖ in units of joules per kilogram can be written as

$$\mathrm{KE}^\varpi = \frac{1}{2}\hat{\mathbf{v}}_h^{\sim\varpi} \cdot \hat{\mathbf{v}}_h^{\sim\varpi}, \quad \text{and} \tag{A11}$$

$$\mathrm{APE}^\varpi = \frac{1}{2}\frac{g^2}{\rho_0^2 N^2}(\hat{\rho}^{\sim\varpi})^2. \tag{A12}$$

By taking the MWT on both sides of Eqs. (A7) and (A10) and multiplying each equation by $\hat{\mathbf{v}}^{\sim\varpi}$ and $(g^2/\rho_0^2 N^2)\hat{\rho}^{\sim\varpi}$, the multiscale KE and APE equations can be written as

$$\frac{\partial \mathrm{KE}^\varpi}{\partial t} = -\nabla \cdot \mathbf{Q}_K^\varpi + \Gamma_K^\varpi - \nabla \cdot \mathbf{Q}_P^\varpi - b^\varpi + F_K^\varpi, \quad \text{and} \tag{A13}$$

$$\frac{\partial \mathrm{APE}^\varpi}{\partial t} = -\nabla \cdot \mathbf{Q}_A^\varpi + \Gamma_A^\varpi + b^\varpi + S_A^\varpi + F_A^\varpi. \tag{A14}$$

The expressions and physical meanings of each term in Eqs. (A13) and (A14) are listed in Table A1, and the detailed derivations are given in Liang (2016). Unlike existing empirical

formalisms, the transfers Γ_n^ϖ to window ϖ at time step n, which represent the local cross-scale energy transfers due to baroclinic/barotropic instabilities, have a very important property:

$$\sum_\varpi \sum_n \Gamma_n^\varpi = 0. \tag{A15}$$

That is, a perfect transfer process only redistributes energy among scale windows, without generating or destroying energy. For this reason, it has been called a *canonical transfer*, in contrast to those defined in previous studies. Note that the forcing and dissipation processes (represented by the F terms) are not explicitly calculated but are considered as the residual terms in this study. For convenience, the transport terms $-\nabla \cdot \mathbf{Q}_K^\varpi$, $-\nabla \cdot \mathbf{Q}_P^\varpi$, and $-\nabla \cdot \mathbf{Q}_A^\varpi$ are expressed as ΔQ_K^ϖ, ΔQ_P^ϖ, and ΔQ_A^ϖ, respectively. The transfers Γ_K^ϖ and Γ_A^ϖ can be further decomposed into three terms ($\Gamma^{0\leftrightarrow1}$, $\Gamma^{1\leftrightarrow2}$, and $\Gamma^{0\leftrightarrow2}$) to represent interactions between different windows. Fig. A1 shows a schematic illustration of the energy cycle for the local ocean domain in a three-window framework. As mentioned by Liang (2016), the transfers bridge different windows and represent interscale processes such as instabilities, whereas the buoyancy conversion and transport function only within each individual window. The former link the KE and APE, and the latter allow communication between different spatial locations.

REFERENCES

Cai, Z., and J. Gan, 2020: Dynamics of the cross-layer exchange for the layered circulation in the South China Sea. *J. Geophys. Res. Oceans*, **125**, e2020JC016131, https://doi.org/10.1029/2020JC016131.

——, ——, Z. Liu, C. R. Hui, and J. Li, 2020: Progress on the formation dynamics of the layered circulation in the South China Sea. *Prog. Oceanogr.*, **181**, 102246, https://doi.org/10.1016/j.pocean.2019.102246.

Chen, G., and H. Xue, 2014: Westward intensification in marginal seas. *Ocean Dyn.*, **64**, 337–345, https://doi.org/10.1007/s10236-014-0691-z.

——, Y. Hou, and X. Chu, 2011: Mesoscale eddies in the South China Sea: Mean properties, spatiotemporal variability, and impact on thermohaline structure. *J. Geophys. Res.*, **116**, C06018, https://doi.org/10.1029/2010JC006716.

Chen, X., and K. Tung, 2014: Varying planetary heat sink led to global-warming slowdown and acceleration. *Science*, **345**, 897–903, https://doi.org/10.1126/science.1254937.

Cummings, J. A., 2005: Operational multivariate ocean data assimilation. *Quart. J. Roy. Meteor. Soc.*, **131**, 3583–3604, https://doi.org/10.1256/qj.05.105.

——, and O. M. Smedstad, 2013: Variational data assimilation for the global ocean. *Data Assimilation for Atmospheric, Oceanic and Hydrologic Applications*, Vol. II, Springer, 303–343.

Gan, J., Z. Liu, and C. Hui, 2016: A three-layer alternating spinning circulation in the South China Sea. *J. Phys. Oceanogr.*, **46**, 2309–2315, https://doi.org/10.1175/JPO-D-16-0044.1.

Gordon, A. L., B. A. Huber, E. J. Metzger, R. D. Susanto, H. E. Hurlburt, and T. R. Adi, 2012: South China Sea throughflow impact on the Indonesian Throughflow. *Geophys. Res. Lett.*, **39**, L11602, https://doi.org/10.1029/2012GL052021.

Hamilton, P., 1990: Deep currents in the Gulf of Mexico. *J. Phys. Oceanogr.*, **20**, 1087–1104, https://doi.org/10.1175/1520-0485(1990)020<1087:DCITGO>2.0.CO;2.

——, 2007: Deep-current variability near the Sigsbee Escarpment in the Gulf of Mexico. *J. Phys. Oceanogr.*, **37**, 708–726, https://doi.org/10.1175/JPO2998.1.

——, 2009: Topographic Rossby waves in the Gulf of Mexico. *Prog. Oceanogr.*, **82** (1), 1–31, https://doi.org/10.1016/j.pocean.2009.04.019.

——, A. Bower, H. Furey, R. Leben, and P. Pérez-Brunius, 2019: The Loop Current: Observations of deep eddies and topographic waves. *J. Phys. Oceanogr.*, **49**, 1463–1483, https://doi.org/10.1175/JPO-D-18-0213.1.

Hogg, N. G., 1981: Topographic waves along 70°W on the continental rise. *J. Mar. Res.*, **39**, 627–649.

——, 2000: Low-frequency variability on the western flanks of the Grand Banks. *J. Mar. Res.*, **58**, 523–545, https://doi.org/10.1357/002224000321511007.

Huang, X., Q. Wang, W. Zhou, and S. Zhou, 2017: Model diagnostic analysis of cross-shelf flow in the northern South China Sea (in Chinese with English abstract). *Chin. Sci. Bull.*, **62**, 1059–1070, https://doi.org/10.1360/N972016-00570.

Johns, W. E., and D. R. Watts, 1986: Time scales and structure of topographic Rossby waves and meanders in the deep Gulf Stream. *J. Mar. Res.*, **44**, 267–290, https://doi.org/10.1357/002224086788405356.

Kawano, T., M. Fukasawa, S. Kouketsu, H. Uchida, T. Doi, I. Kaneko, M. Aoyama, and W. Schneider, 2006: Bottom water warming along the pathway of lower circumpolar deep water in the Pacific Ocean. *Geophys. Res. Lett.*, **33**, L23613, https://doi.org/10.1029/2006GL027933.

LaCasce, J. H., 1998: A geostrophic vortex over a slope. *J. Phys. Oceanogr.*, **28**, 2362–2381, https://doi.org/10.1175/1520-0485(1998)028<2362:AGVOAS>2.0.CO;2.

——, J. Escartin, E. P. Chassignet, and X. Xu, 2019: Jet instability over smooth, corrugated, and realistic bathymetry. *J. Phys. Oceanogr.*, **49**, 585–605, https://doi.org/10.1175/JPO-D-18-0129.1.

Lan, J., N. Zhang, and Y. Wang, 2013: On the dynamics of the South China Sea deep circulation. *J. Geophys. Res. Oceans*, **118**, 1206–1210, https://doi.org/10.1002/jgrc.20104.

Li, M., J. Wei, D. Wang, A. L. Gordon, S. Yang, P. Malanotte-Rizzoli, and G. Jiang, 2019: Exploring the importance of the Mindoro-Sibutu pathway to the upper layer circulation of the South China Sea and the Indonesian Throughflow. *J. Geophys. Res. Oceans*, **124**, 5054–5066, https://doi.org/10.1029/2018JC014910.

Liang, X. S., 2016: Canonical transfer and multiscale energetics for primitive and quasigeostrophic atmospheres. *J. Atmos. Sci.*, **73**, 4439–4468, https://doi.org/10.1175/JAS-D-16-0131.1.

Liang, X., and D. G. M. Anderson, 2007: Multiscale window transform. *Multiscale Model. Simul.*, **6**, 437–467, https://doi.org/10.1137/06066895X.

Luecke, C. A., and Coauthors, 2017: The global mesoscale eddy available potential energy field in models and observations. *J. Geophys. Res. Oceans*, **122**, 9126–9143, https://doi.org/10.1002/2017JC013136.

Ma, Q., F. Wang, J. Wang, and Y. Lyu, 2019: Intensified deep ocean variability induced by topographic Rossby waves at the Pacific Yap-Mariana Junction. *J. Geophys. Res. Oceans*, **124**, 8360–8374, https://doi.org/10.1029/2019JC015490.

Magalhães, F. C., J. L. L. Azevedo, and L. R. Oliveira, 2017: Energetics of eddy-mean flow interactions in the Brazil Current between 20°S and 36°S. *J. Geophys. Res. Oceans*, **122**, 6129–6146, https://doi.org/10.1002/2016JC012609.

Maslo, A., J. M. A. C. De Souza, and J. S. Pardo, 2020: Energetics of the deep Gulf of Mexico. *J. Phys. Oceanogr.*, **50**, 1655–1675, https://doi.org/10.1175/JPO-D-19-0308.1.

Meinen, C., E. Fields, R. S. Pickart, and D. R. Watts, 1993: Ray tracing on topographic Rossby waves. University of Rhode Island Graduate School of Oceanography Tech. Rep. 93-1, 43 pp.

Nan, F., H. Xue, F. Chai, L. Shi, M. Shi, and P. Guo, 2011: Identification of different types of Kuroshio intrusion into the South China Sea. *Ocean Dyn.*, **61**, 1291–1304, https://doi.org/10.1007/s10236-011-0426-3.

——, ——, and F. Yu, 2015: Kuroshio intrusion into the South China Sea: A review. *Prog. Oceanogr.*, **137**, 314–333, https://doi.org/10.1016/j.pocean.2014.05.012.

Oey, L. Y., 2008: Loop Current and deep eddies. *J. Phys. Oceanogr.*, **38**, 1426–1449, https://doi.org/10.1175/2007JPO3818.1.

——, and H. C. Lee, 2002: Deep eddy energy and topographic Rossby waves in the Gulf of Mexico. *J. Phys. Oceanogr.*, **32**, 3499–3527, https://doi.org/10.1175/1520-0485(2002)032<3499:DEEATR>2.0.CO;2.

Olbers, D., J. Willebrand, and C. Eden, 2012: *Ocean Dynamics*. Spring-Verlag, 704 pp.

Pedlosky, J., 2003: *Waves in the Ocean and Atmosphere: Introduction to Wave Dynamics*. Springer-Verlag, 260 pp.

Peña-Molino, B., T. M. Joyce, and J. M. Toole, 2012: Variability in the deep western boundary current: Local versus remote forcing. *J. Geophys. Res.*, **117**, C12022, https://doi.org/10.1029/2012JC008369.

Pickart, R. S., 1995: Gulf Stream–generated topographic Rossby waves. *J. Phys. Oceanogr.*, **25**, 574–586, https://doi.org/10.1175/1520-0485(1995)025<0574:GSTRW>2.0.CO;2.

——, and D. R. Watts, 1990: Deep western boundary current variability at Cape Hatteras. *J. Mar. Res.*, **48**, 765–791, https://doi.org/10.1357/002224090784988674.

Qu, T., Y. Du, and H. Sasaki, 2006: South China Sea throughflow: A heat and freshwater conveyor. *Geophys. Res. Lett.*, **33**, L23617, https://doi.org/10.1029/2006GL028350.

Quan, Q., and H. Xue, 2018: Layered model and insights into the vertical coupling of the South China Sea circulation in the upper and middle layers. *Ocean Modell.*, **129**, 75–92, https://doi.org/10.1016/j.ocemod.2018.06.006.

——, and ——, 2019: Influence of abyssal mixing on the multilayer circulation in the South China Sea. *J. Phys. Oceanogr.*, **49**, 3045–3060, https://doi.org/10.1175/JPO-D-19-0020.1.

Reid, R., and O. Wang, 2004: Bottom-trapped Rossby waves in an exponentially stratified ocean. *J. Phys. Oceanogr.*, **34**, 961–967, https://doi.org/10.1175/1520-0485(2004)034<0961:BRWIAE>2.0.CO;2.

Rhines, P. B., 1970: Edge-, bottom-, and Rossby waves in a rotating stratified fluid. *Geophys. Fluid Dyn.*, **1**, 273–302, https://doi.org/10.1080/03091927009365776.

——, and F. Bretherton, 1973: Topographic Rossby waves in a rough-bottomed ocean. *J. Fluid Mech.*, **61**, 583–607, https://doi.org/10.1017/S002211207300087X.

Siedler, G., J. Holfort, W. Zenk, T. J. Müller, and T. Csernok, 2004: Deep-water flow in the Mariana and Caroline Basins. *J. Phys. Oceanogr.*, **34**, 566–581, https://doi.org/10.1175/2511.1.

Shu, Y., H. Xue, D. Wang, F. Chai, Q. Xie, J. Yao, and J. Xiao, 2014: Meridional overturning circulation in the South China Sea envisioned from the high-resolution global reanalysis data GLBa0.08. *J. Geophys. Res. Oceans*, **119**, 3012–3028, https://doi.org/10.1002/2013JC009583.

——, and Coauthors, 2016: Persistent and energetic bottom-trapped topographic Rossby waves observed in the southern South China Sea. *Sci. Rep.*, **6**, 24338, https://doi.org/10.1038/srep24338.

Thompson, R. O. R. Y., 1977: Observations of Rossby waves near site D. *Prog. Oceanogr.*, **7**, 135–162, https://doi.org/10.1016/0079-6611(77)90003-9.

——, and J. Luyten, 1976: Evidence for bottom-trapped topographic Rossby waves from single moorings. *Deep-Sea Res.*, **23**, 629–635, https://doi.org/10.1016/0011-7471(76)90005-X.

Wang, D. P., and C. N. K. Mooers, 1976: Coastal-trapped waves in a continuously stratified ocean. *J. Phys. Oceanogr.*, **6**, 853–863, https://doi.org/10.1175/1520-0485(1976)006<0853:CTWIAC>2.0.CO;2.

Wang, D. X., J. Xiao, Y. Shu, Q. Xie, J. Chen, and Q. Wang, 2016: Progress on deep circulation and meridional overturning circulation in the South China Sea. *Sci. Chin*, **59**, 1827–1833, https://doi.org/10.1007/s11430-016-5324-6.

Wang, G., S. Xie, T. Qu, and R. Huang, 2011: Deep South China Sea circulation. *Geophys. Res. Lett.*, **38**, L05601, https://doi.org/10.1029/2010GL046626.

Wang, Q., and Coauthors, 2019: Energetic topographic Rossby waves in the northern South China Sea. *J. Phys. Oceanogr.*, **49**, 2697–2714, https://doi.org/10.1175/JPO-D-18-0247.1.

Xie, Q., J. Xiao, D. Wang, and Y. Yu, 2013: Analysis of deep-layer and bottom circulations in the South China Sea based on eight quasi-global ocean model outputs. *Chin. Sci. Bull.*, **58**, 4000–4011, https://doi.org/10.1007/s11434-013-5791-5.

Xiu, P., F. Chai, L. Shi, H. Xue, and Y. Chao, 2010: A census of eddy activities in the South China Sea during 1993–2007. *J. Geophys. Res.*, **115**, C03012, https://doi.org/10.1029/2009JC005657.

Xu, F., and L. Y. Oey, 2014: State analysis using the Local Ensemble Transform Kalman Filter (LETKF) and the three-layer circulation structure of the Luzon Strait and the South China Sea. *Ocean Dyn.*, **64**, 905–923, https://doi.org/10.1007/s10236-014-0720-y.

Yang, Y., and X. S. Liang, 2018: On the seasonal eddy variability in the Kuroshio Extension. *J. Phys. Oceanogr.*, **48**, 1675–1689, https://doi.org/10.1175/JPO-D-18-0058.1.

——, R. H. Weisberg, Y. Liu, and X. S. Liang, 2020: Instabilities and multiscale interactions underlying the Loop Current eddy shedding in the Gulf of Mexico. *J. Phys. Oceanogr.*, **50**, 1289–1317, https://doi.org/10.1175/JPO-D-19-0202.1.

Yu, Z., S. Shen, J. P. McCreary, M. Yaremchuk, and R. Furue, 2007: South China Sea throughflow as evidenced by satellite images and numerical experiments. *Geophys. Res. Lett.*, **34**, L01601, https://doi.org/10.1029/2006GL028103.

Zhang, Z., W. Zhao, B. Qiu, and J. Tian, 2017: Anticyclonic eddy sheddings from Kuroshio Loop and the accompanying cyclonic eddy in the northeastern South China Sea. *J. Phys. Oceanogr.*, **47**, 1243–1259, https://doi.org/10.1175/JPO-D-16-0185.1.

Zhao, B., and M.-L. Timmermans, 2018: Topographic Rossby waves in the Arctic Ocean's Beaufort Gyre. *J. Geophys. Res. Oceans*, **123**, 6521–6530, https://doi.org/10.1029/2018JC014233.

Zhou, C., W. Zhao, J. Tian, X. Zhao, Y. Zhu, Q. Yang, and T. Qu, 2017: Deep western boundary current in the South China Sea. *Sci. Rep.*, **7**, 9303, https://doi.org/10.1038/s41598-017-09436-2.

Zhu, Y., J. Sun, Y. Wang, Z. Wei, D. Yang, and T. Qu, 2017: Effect of potential vorticity flux on the circulation in the South China Sea. *J. Geophys. Res. Oceans*, **122**, 6454–6469, https://doi.org/10.1002/2016JC012375.